

Quantum saturation and condensation of excitons in Cu_2O : A theoretical study

G. M. Kavoulakis, Gordon Baym, and J. P. Wolfe

Department of Physics, University of Illinois at Urbana-Champaign, 1110 West Green Street, Urbana, Illinois 61801

(Received 6 June 1995)

Recent experiments on high density excitons in Cu_2O provide evidence for degenerate quantum statistics and Bose-Einstein condensation of this nearly ideal gas. We model the time dependence of this bosonic system including exciton decay mechanisms, energy exchange with phonons, and interconversion between ortho (triplet-state) and para (singlet-state) excitons, using parameters for the excitonic decay, the coupling to acoustic and low-lying optical phonons, Auger recombination, and ortho-para interconversion derived from experiment. The single adjustable parameter in our model is the optical-phonon cooling rate for Auger and laser-produced hot excitons. We show that the ortho excitons move along the phase boundary without crossing it (i.e., they exhibit a “quantum saturation”), as a consequence of the balance of entropy changes due to cooling of excitons by phonons and heating by the nonradiative Auger two-exciton recombination process. The Auger annihilation rate for para-para collisions is much smaller than that for ortho-para and ortho-ortho collisions, explaining why, under the given experimental conditions, the para excitons condense while the ortho excitons fail to do so.

I. INTRODUCTION

While Bose-Einstein condensation underlies the remarkable properties of the strongly interacting superfluid, liquid helium II, discovery of Bose-Einstein condensation in nearly ideal gases has proven difficult. Many recent experiments have focussed on this challenge.¹⁻³ In the semiconductor Cu_2O , excitons (electron-hole pairs bound by their Coulomb attraction) have exhibited Bose-Einstein statistics^{4,5} and, indeed, Bose-Einstein condensation.^{6,7} In these experiments, intense pulses of laser light excite the crystal, creating a gas of (spin-triplet) ortho excitons and (spin-singlet) para excitons, split by an exchange energy $\Delta E \approx 12$ meV.^{8,9} The kinetic-energy distribution of ortho excitons as a function of time from the onset of the laser pulse is observed by spectroscopy of their photoluminescence (considerably more intense than that of the para excitons). In the classical (low-density) regime, the energy distribution is observed to be Maxwell-Boltzmann, described by an effective exciton temperature. In the quantum (high-density) regime, the spectra exhibit Bose-Einstein distributions, as shown in Figs. 1(a)–1(c). These spectra are well fit in terms of an ideal gas with an instantaneous chemical potential μ and temperature T . From these parameters, one can directly calculate the density of the gas.

The densities obtained from the recombination spectra of Snoke *et al.* are plotted in Fig. 1(d). This figure shows the experimental results with a long (10-ns) laser pulse (black dots) and with a short (100-ps) laser pulse (open circles). These experiments observe a “quantum saturation” of the (spin-triplet) orthoexcitons, i.e., a tendency for them to move closely parallel to the critical line without condensing.⁵ The critical line, an adiabat (constant entropy per particle, $s = S/N$), has the form, $T_c = (2\pi\hbar^2/mk_B)[n/g\zeta(3/2)]^{2/3}$, where the degeneracy $g=3$ for orthoexcitons and 1 for para excitons. We note that lines in the phase diagram parallel (in a log-log plot) to the condensation line at higher temperature correspond to adiabats, along which $\alpha \equiv -\mu/k_B T$ is con-

stant, since s is only a function of α for an ideal Bose gas.

Experimental measurements of the para excitons indicate condensation of this component in unstressed⁶ and uniaxially stressed crystals.⁷ The stressed results are summarized in Figs. 2(a,b). At high densities the orthoexcitons decay very rapidly, due, as we shall see, to Auger recombination and ortho-to-para conversion. In contrast, the para excitons decay very slowly even at high densities. Figure 2(b) shows density-temperature trajectories for both ortho excitons (open circles) and para excitons (black dots) for long pulses. The stress splits the triply degenerate ortho-exciton level into three components and only the lower of the three is significantly populated, leading to a closer proximity to the condensation line than in the unstressed case. No ortho-exciton condensation is observed. The stress, however, does lead to clear evidence in the para-exciton spectrum that the para excitons condense: their energy distribution is much sharper than that of the ortho excitons at a given time. Under these conditions the para exciton density is determined from the relative intensities of ortho excitons and para excitons, combined with the spectroscopically determined density of the orthoexcitons. This analysis yields the striking evidence for para-exciton condensation shown in Fig. 2(b).

The nonstressed para-exciton spectrum also displays anomalies which are interpreted as a result of condensation but are not so cleanly analyzed: a highly blueshifted component is observed which may indicate a superfluid with a large drift velocity. The exact effect of the stress is not well understood, but it is possible that it helps to localize better the two components of the gas, making the analysis more straightforward.¹⁰

In this study we identify the salient factors that lead to the quantum saturation of ortho excitons. We find, by quantitative investigation of the system, that the observed behavior can be understood in terms of well-established kinetic processes of cooling, reheating, ortho-para conversions, and recombination of the excitons. The essence of the argument is

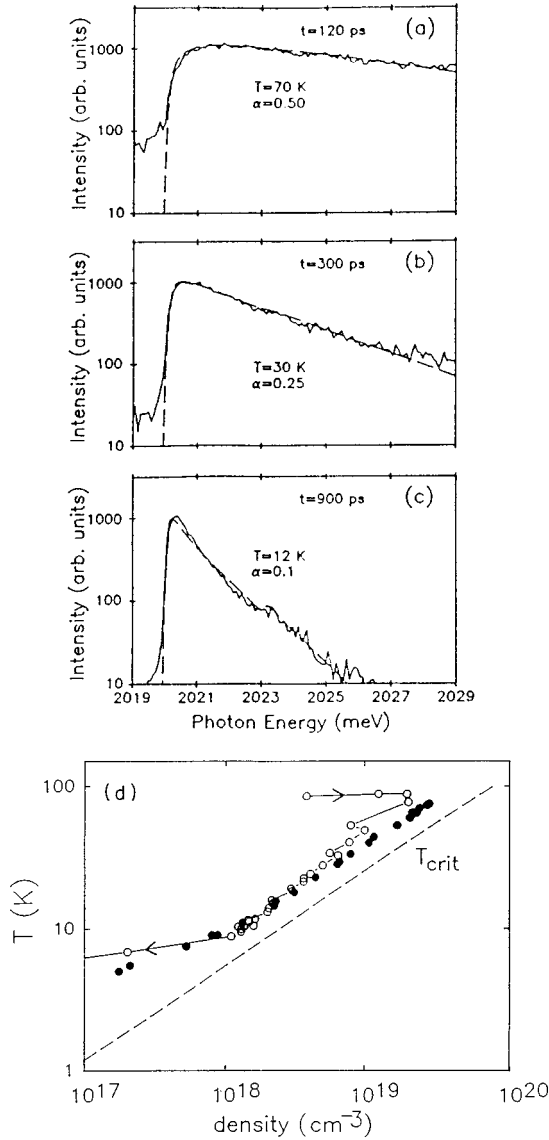


FIG. 1. (a)–(c) The LO phonon-assisted recombination spectrum of ortho excitons for three different times following a 100-ps laser pulse. The data are fitted by Bose-Einstein distributions (dashed lines). Temperatures and densities extracted from the fits to the photoluminescence spectra. (d) Open circles show the density of ortho excitons at various times calculated from experimentally determined μ and T , as a function of temperature, for short laser pulses. Black dots are the results for ortho excitons in the long-pulse (10-ns) case. In both experiments the ortho excitons move along the critical line for condensation, without condensing. All data are from Snoke *et al.*, Refs. 5, 6, and 13.

that the rate of change of the entropy of the excitons is a balance between the entropy loss due to phonon cooling and heating following Auger annihilation of exciton pairs into hot electrons and holes. The rate of phonon cooling, which is dominated by emission of acoustic phonons, varies as $aT^{3/2}$ for exciton temperatures that are large compared with the ambient lattice temperature. On the other hand, heating of the excitons from the Auger process has, as we shall see, the form bn_o proportional to the density of ortho excitons, n_o . Thus the time rate of change of the ortho-exciton entropy per particle, s_o , is given in first approximation by

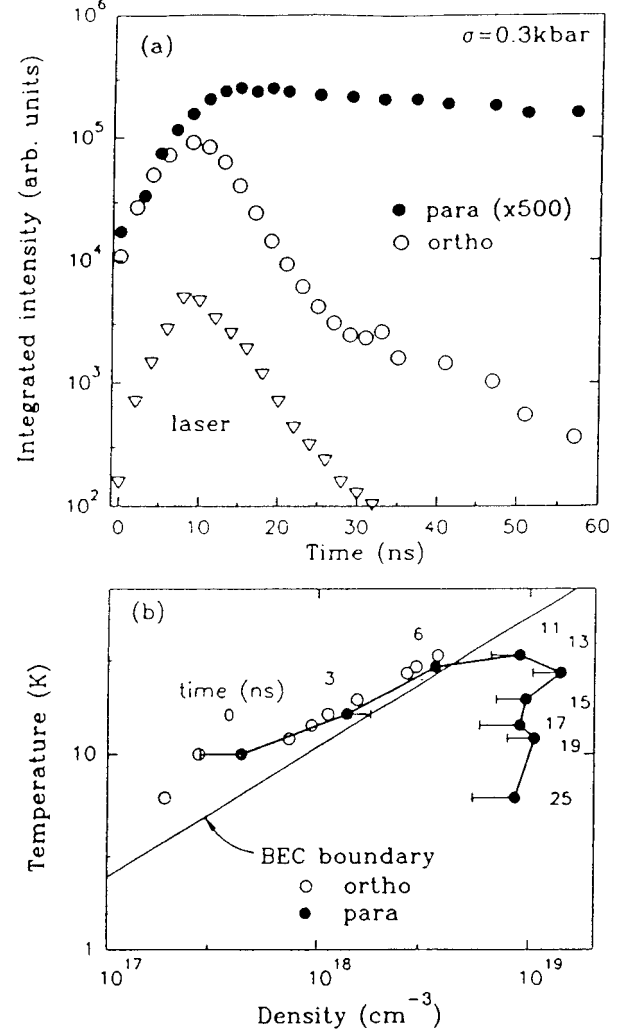


FIG. 2. (a) Data from lightly stressed crystals with long-pulse (10-ns) excitation (Ref. 7). The laser profile (triangles), the number of ortho excitons in the lowest ortho-exciton level (open circles), and the number of para excitons (black dots) as function of time. The para excitons show a significantly smaller decay rate. (b) Corresponding trajectories for ortho excitons (open circles) and para excitons (black dots) in the density-temperature plane. The straight line is the condensation phase boundary, which is identical for para excitons and ortho excitons in the stressed case. Note that the para excitons are in the condensed region at times later than 8 ns.

$$T \frac{ds_o}{dt} = -aT^{3/2} + bn_o. \quad (1)$$

Note that the right side vanishes along the adiabat given by $T^{3/2}/n_o = b/a$, which is a stable fixed point of this equation; e.g., if the temperature is too high, phonon cooling will increase, pulling the entropy down to this adiabat, etc. As we see in Sec. VI C, where we present this argument in greater detail, the stable adiabat is only slightly above the condensation line. Our qualitative and quantitatively detailed explanation of the quantum saturation indicates that we have identified the critical mechanisms of the exciton dynamics, enabling us to explain why confidence that the para excitons do indeed condense under the experimental conditions.

We model the time evolution of the gas from a rate equation approach. In Sec. II we construct the rate equations that incorporate the relevant dynamical processes, which we examine individually in Secs. III–V. In Sec. III we consider exciton-phonon interactions and show how the onset of quantum statistics tends to suppress these cooling processes. The effects of ortho-para conversion mechanisms^{11,12} are considered in Sec. IV. We find that the ortho-para conversion process is strongly modified for excitons in the condensed phase. We examine in Sec. V the Auger-decay process, in which two excitons annihilate to form an ionized electron-hole pair,¹³ with the ionized electrons and holes subsequently recombining into excitons. This process tends to keep the gas away from the degenerate region both by decreasing the exciton density and by indirectly heating the excitons. At high densities the ortho excitons decay very rapidly due to Auger recombination and ortho-to-para conversion; however, as we show, the striking longevity of the para excitons, which is crucial to their ability to cross the Bose-Einstein condensation boundary as seen in Fig. 2(b), is due to the weakness of the para-para Auger process. This weakness is a result of the detailed band structure. In Sec. VI an analysis of the solutions to the rate equations for a range of values of the input parameters allows us to see the relative importance of the various physical processes in producing the quantum saturation and condensation effects. In the same section we discuss the evolution of the ortho-exciton entropy, and calculate the time for the ortho-excitons to approach the adiabat of stability. Finally, in Sec. VII we summarize our conclusions.

II. RATE EQUATIONS

We treat the exciton gas as nearly ideal, and kept in thermal equilibrium by the rapid exciton-exciton collisions, with a single temperature T , generally greater than the lattice temperature T_{ℓ} . For example, for excitons scattering as hard spheres with a scattering radius on the order of the exciton Bohr radius, the characteristic scattering time is a few picoseconds for typical densities 10^{18} – 10^{19} cm^{-3} . The slower interconversion processes between the ortho excitons and para excitons do not allow them to come into chemical equilibrium quickly, so that, in general, the chemical potential of the ortho excitons μ_o differs from that of the para excitons μ_p . We further assume that the lattice maintains a constant temperature T_{ℓ} throughout the relaxation process. At 30–50 ns after an intense 10-ns pulse the excitons assume a temperature ~ 5 – 6 K, which we conclude is the lattice temperature in the excitation region at that time, somewhat higher than that of the surrounding cold lattice and the bath temperature (2 K).

In the experiments, photoexcitation by green laser light creates hot electrons and holes within about a micrometer of the crystal surface. These hot carriers diffuse and within a nanosecond relax to form the excitons under study. During the first 5–20 ns the spatial extent of the excitonic gas under consideration has been experimentally estimated to be about 30 μm . We make the simplifying assumption that the excitonic gas occupies a constant volume over the entire time interval, which is valid at least for the first 7 ns. Going beyond this approximation to include the full hydrodynamics of expansion is a task for a future paper (see Ref. 14 for an

initial approach). We also neglect inhomogeneities in the exciton gas and assume that the ortho excitons and para excitons occupy the same volume. The parameters of the problem, all time dependent, are therefore the exciton temperature T , the number of ortho excitons N_o , and the number of paraexcitons N_p .

In the normal (noncondensed) regime the chemical potentials μ_i ($i=o,p$) of each of the species are functions of N_i and T . In the condensed regime, where the chemical potential is zero, we take the number of condensed particles $N_{i,\text{cond}}$ to be the equilibrium result, $N_{i,\text{cond}} = N_i [1 - (T/T_{ci})^{3/2}]$, where T_{ci} is the critical temperature for condensation of the component i .

Excitons are formed by the laser through creation of ionized electrons and holes, with an excess kinetic energy of about 250 meV per pair, which then combine in random spin states to give ortho excitons and para excitons in a three-to-one ratio. The rate equations that describe how the total numbers N_o and N_p of the two species change in time are then

$$\frac{dN_o}{dt} = G_o(t) - \frac{N_o}{\tau_{lo}} - DN_{o,\text{exc}} + UN_{p,\text{exc}} - \frac{N_o}{\tau_{Ao}} + \frac{3}{4} \frac{1}{2} \left(\frac{N_o}{\tau_{Ao}} + \frac{N_p}{\tau_{Ap}} \right), \quad (2)$$

$$\frac{dN_p}{dt} = G_p(t) - \frac{N_p}{\tau_{lp}} + DN_{o,\text{exc}} - UN_{p,\text{exc}} - \frac{N_p}{\tau_{Ap}} + \frac{1}{4} \frac{1}{2} \left(\frac{N_o}{\tau_{Ao}} + \frac{N_p}{\tau_{Ap}} \right), \quad (3)$$

where $G_i(t)$ is the laser production rate of excitons, and the τ_{li} are the intrinsic radiative lifetimes ($\tau_{lo} \approx 300$ ns and $\tau_{lp} \approx 150$ μs). The quantity D is the ortho-to-para down-conversion rate, and U is the para-to-ortho up-conversion rate; as we show later only the noncondensed (nonzero momentum) excitons participate significantly in the ortho-para interconversion processes, so that these terms are effectively proportional to the number of noncondensed, or excited, particles, $N_{i,\text{exc}}$. The terms $-N_i/\tau_{Ai}$ describe the Auger annihilation process, while the final terms account for the reformation of excitons from the Auger-ionized electrons and holes. The factor of 1/2 arises because for each two excitons destroyed by the Auger process; only one reforms, with probability 1/4 to be a para exciton and 3/4 to be an ortho exciton. The right side of these equations is a function of the numbers of excitons N_o , N_p and their common temperature T .

The third kinetic equation is the rate of change of the total internal energy, $E = E_o + E_p$, of the gas

$$\left(\frac{dE}{dt} \right) = \left(\frac{\partial E}{\partial t} \right)_{\text{phonon}} + \left(\frac{\partial E}{\partial t} \right)_{o \rightarrow p} + \left(\frac{\partial E}{\partial t} \right)_{p \rightarrow o} + \left(\frac{\partial E}{\partial t} \right)_L + \left(\frac{\partial E}{\partial t} \right)_A + \left(\frac{\partial E}{\partial t} \right)_I. \quad (4)$$

The terms in this equation describe, respectively, the change in the energy due to collisions of the excitons with the cold lattice (“phonon”), phonon-assisted ortho-para interconver-

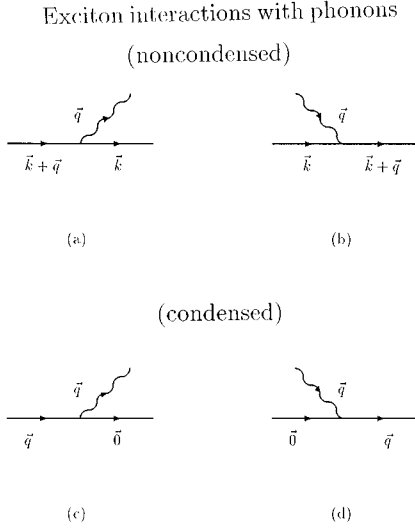


FIG. 3. Exciton-phonon interaction processes for noncondensed (a,b) and condensed (c,d) excitons.

sions, laser heating (L), heating from Auger annihilations (A), and radiative recombination (I). In fact, because the radiative recombination lifetimes τ_{lo} and τ_{lp} are long, the latter process is negligible in the three rate equations. Since E is a function of N_o , N_p , and T , the rate equations can be equivalently cast as equations for the rate of temperature change $\partial T/\partial t$, and the exciton numbers. Let us now examine each of the relaxation mechanisms in turn.

III. PHONON COOLING OF EXCITONS

Excitons in Cu_2O interact with acoustic and optical phonons through a deformation potential interaction.^{15,16} If the gas is above the condensation temperature T_c , the rate of change of the energy of the exciton gas for the processes in which an exciton emits or absorbs a phonon, shown in Figs. 3(a,b), is

$$\left(\frac{\partial E}{\partial t}\right)_{\text{phonon}} = \frac{2\pi}{\hbar} \sum_{\mathbf{k}, \mathbf{q}} |M_{\mathbf{q}}|^2 \{n_{\mathbf{k}}(1+n_{\mathbf{k}+\mathbf{q}})f_{\mathbf{q}} - n_{\mathbf{k}+\mathbf{q}}(1+n_{\mathbf{k}}) \times (1+f_{\mathbf{q}})\} \hbar \omega_{\mathbf{q}} \delta(\varepsilon_{\mathbf{k}+\mathbf{q}} - \varepsilon_{\mathbf{k}} - \hbar \omega_{\mathbf{q}}); \quad (5)$$

here $n_{\mathbf{k}}$ is the (ortho or para) exciton distribution, $f_{\mathbf{q}}$ is the phonon distribution, $M_{\mathbf{q}}$ is the exciton-phonon interaction matrix element, $\varepsilon_{\mathbf{k}}$ is the exciton energy, and $\hbar \omega_{\mathbf{q}}$ the phonon energy. Below T_c , the ground state is occupied by a macroscopic number of particles, so that we have an additional contribution, Figs. 3(c,d), from condensed particles:

$$\left(\frac{\partial E}{\partial t}\right)_{\text{phonon}}^{\text{cond}} = \frac{2\pi}{\hbar} \sum_{\mathbf{q}} |M_{\mathbf{q}}|^2 \{N_{\text{cond}}(1+n_{\mathbf{q}})f_{\mathbf{q}} - (1+N_{\text{cond}})n_{\mathbf{q}}(1+f_{\mathbf{q}})\} \hbar \omega_{\mathbf{q}} \delta(\varepsilon_{\mathbf{q}} - \hbar \omega_{\mathbf{q}}). \quad (6)$$

We define the exciton gas structure factor,

$$S(\mathbf{q}, \omega) = \sum_{\mathbf{k}} n_{\mathbf{k}}(1+n_{\mathbf{k}+\mathbf{q}}) \delta(\varepsilon_{\mathbf{k}+\mathbf{q}} - \varepsilon_{\mathbf{k}} - \hbar \omega), \quad (7)$$

in terms of which Eq. (5) takes the form

$$\left(\frac{\partial E}{\partial t}\right)_{\text{phonon}} = \frac{2\pi}{\hbar} \sum_{\mathbf{q}} |M_{\mathbf{q}}|^2 \hbar \omega_{\mathbf{q}} S(\mathbf{q}, \omega_{\mathbf{q}}) f_{\mathbf{q}} (1 - e^{(\beta_{\neq} - \beta) \hbar \omega_{\mathbf{q}}}), \quad (8)$$

where $\beta_{\neq} = 1/k_B T_{\neq}$ and $\beta = 1/k_B T$. In terms of $v_{\pm} \equiv \beta[(\hbar^2/2m)(q/2 \pm m\omega/\hbar q)^2 - \mu]$, the structure factor becomes

$$S(\mathbf{q}, \omega) = \frac{V}{4\pi^2} \frac{m^2}{\beta \hbar^4 q} \frac{1}{(1 - e^{-\beta \hbar \omega})} \ln \left(\frac{1 - e^{-v_+}}{1 - e^{-v_-}} \right), \quad (9)$$

where V is the volume of the exciton gas and m is the exciton mass, $\approx (3.0 \pm 0.2)m_e^0$ (where m_e^0 is the bare electron mass)^{17,18} for the ortho excitons; in this analysis we assume that both the ortho excitons and the para excitons have the same mass (see next paragraph) and let $\varepsilon_{\mathbf{k}} = E_g - E_b + \Delta E + \hbar^2 k^2/2m$, where E_g is the energy-gap (≈ 2.17 eV in Cu_2O), E_b is the binding energy, and ΔE is the exchange energy (in which an exciton virtually annihilates and reforms), which is nonzero for the ortho excitons and zero for the para excitons.

Our choice of the effective masses is based on the experimentally known Rydberg of 97 meV for the excited exciton states, which depends on the reduced mass of the electron and the hole and the dielectric constant of the material. A range of values for the effective electron and hole masses have been reported,^{20,21} and there are also uncertainties in the dielectric constant.¹⁹ The present calculation is not critically sensitive to the choice of masses and dielectric constant, so we choose the measured values $m_e = 0.84m_e^0$, $m_h = 0.61m_e^0$, and $\epsilon_0 = 7.11$ (Ref. 19) for the static dielectric constant, which yield the excitonic Rydberg ≈ 99 meV, very close to the experimental value obtained from the absorption spectrum of the excited excitonic states. The total ortho-exciton mass is not equal to the sum of the effective electron and hole masses m_i , likely due to the central cell corrections,¹⁷ i.e., the corrections due to the fact that the Bohr radius is comparable with the lattice constant. The central cell corrections are also likely the reason that the binding energy of the $1s$ state (approximately 153 meV) is much larger than the Rydberg for the excited excitonic states. This measured binding energy corresponds to a Bohr radius $a = e^2/2\epsilon_0 E_b \approx 7$ Å, where E_b is the exciton binding energy.

For acoustic phonons $\omega_{\mathbf{q}} = v_{\neq} q$, where v_{\neq} is the longitudinal sound velocity. We neglect the interaction of excitons with acoustic transverse phonons, since it is about 50 times weaker than that with the longitudinal phonons.^{17,23} The square of the matrix element for deformation potential scattering is¹⁶

$$|M_{\mathbf{q}}^{ac}|^2 = \frac{\hbar D_a^2 q}{2\rho V v_{\neq}} \frac{1}{[1 + (qa/4)^2]^4}, \quad (10)$$

where D_a is the acoustic deformation potential, ≈ 1.8 eV experimentally,¹⁸ a is the exciton Bohr radius, q is the phonon wave vector, and $\rho \approx 6.0$ gm/cm³ is the mass density of the material. The quantity $[1 + (qa/4)^2]^4$ in the denominator

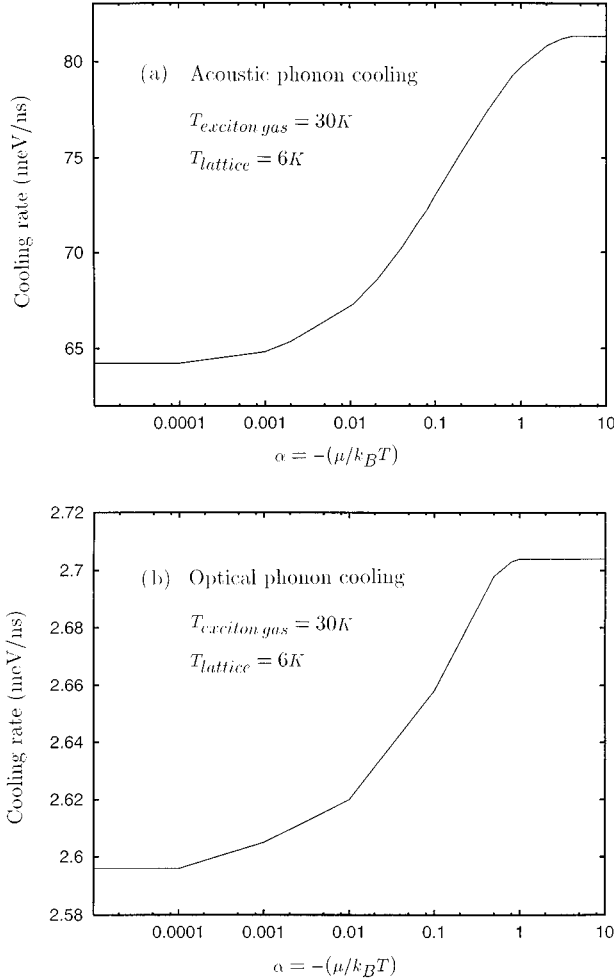


FIG. 4. Acoustic- and optical-phonon cooling rates per exciton as a function of α for fixed exciton gas temperature 30 K and lattice temperature 6 K. Increased degeneracy (smaller α) lowers the cooling rate.

of Eq. (10) comes from the square of the Fourier transform of the relative $1s$ electron-hole wave function, evaluated at $m_e = m_h$, where m_i are the effective electron and hole masses. This correction term becomes significant when the wavelength of the phonon is comparable to the Bohr radius, and is actually negligible for thermalized excitons with $T \leq 70$ K, cf. Ref. 18.

Combining Eqs. (8) and (10), we find the rate of acoustic-phonon cooling per exciton,

$$\begin{aligned} \frac{1}{N} \left(\frac{\partial E}{\partial t} \right)_{\text{LA}} = & - \frac{(mv_\ell^2)^2}{\hbar} \frac{1}{8\pi^3} \frac{m}{m_{\text{ion}}} \frac{1}{na^3} \left(\frac{a}{a_\ell} \right)^3 \\ & \times \frac{(k_B T)^5 D_a^2}{(\hbar v_\ell / a_\ell)^6 (mv_\ell^2)} \int_0^\infty dx x^3 \left[\frac{1}{e^x - 1} \right. \\ & \left. - \frac{1}{e^{xT/T_\ell} - 1} \right] \frac{1}{(1 + [k_B T a x / 4 \hbar v_\ell]^2)^4} \\ & \times \ln \left(\frac{1 - e^{-y_+}}{1 - e^{-y_-}} \right), \end{aligned} \quad (11)$$

where $n = N/V$ is the density of excitons, $a_\ell = 4.26 \text{ \AA}$ is the lattice constant, $m_{\text{ion}} \equiv \rho a_\ell^3$ is a mean ion mass, and $a \approx 7 \text{ \AA}$

for the ground state. The factors v_\pm in Eq. (9) become $y_\pm = (mv_\ell^2 / 8k_B T) [(xk_B T / mv_\ell^2) \pm 2]^2 - \beta\mu$. The prefactor $(mv_\ell^2)^2 / \hbar$ is $\approx 176 \text{ meV/ns}$. Equation (11) depends upon the quantum degeneracy factor, $\alpha \equiv -\mu/k_B T$. Along lines of small constant α , the acoustic-phonon cooling rate per particle, with $D_a = 1.8 \text{ eV}$ from Snoke *et al.*, is

$$\frac{1}{N} \left(\frac{\partial E}{\partial t} \right)_{\text{LA}} \approx -0.49 T^{3/2} (1 - T_\ell / T) \text{ meV/ns}, \quad (12)$$

with T measured in kelvin; in the classical limit, the coefficient becomes 0.62.

Excitons also cool by emission of optical phonons, of which there are 15 modes at the zone center of Cu_2O .²² The optical phonons are: Γ_{25}^- (threefold degenerate, of energy 11.4 meV), Γ_{12}^- (twofold degenerate, of energy 13.8 meV), Γ_{15}^- (threefold degenerate, of energy 18.7 meV), Γ_2^- (nondegenerate, of energy 43 meV), Γ_{15}^+ (threefold degenerate, of energy 64 meV), and Γ_{15}^- (threefold degenerate, of energy 79 meV). They group into two parts; the first eight with relatively lower energies, while the remaining seven have relatively higher energies. In calculating the cooling rate of thermalized excitons we neglect the contribution of the second group; even the lowest ones with $\hbar\omega = 43 \text{ meV}$ corresponding to a Maxwellian temperature of $2\hbar\omega/3k_B \approx 300 \text{ K}$, which suppresses their contribution to exciton cooling. In contrast, these high-energy phonons definitely need to be taken into account in calculating cooling of nonthermalized high-kinetic-energy excitons, Sec. V. All the lower-energy phonons have negative parity, as their group theory notation indicates. Since the parity of the excitons is even, the matrix element for the exciton odd-parity optical phonon interaction vanishes at the zone center. The average squared matrix element for the deformation potential interaction with an optical phonon of frequency ω_i can be written as¹⁶

$$|M_{\mathbf{q}}^{\text{opt}}|^2 = \frac{\hbar D_i^2}{2\rho V \omega_i}, \quad (13)$$

where D_i is the optical phonon deformation potential, averaged over the whole Brillouin zone; for the Γ_{15}^- phonon of zone-center energy 18.7 meV, $D_i \approx 0.17 \text{ eV/\AA}$ in magnitude.¹⁸ As noted in Ref. 18, the ratios of the deformation potentials of the low-energy phonons can be set by comparison with the data of Yu and Shen¹⁷ for the relative efficiency of the three ‘‘three-phonon Raman lines.’’ The heights of these lines, which are simply due to hot luminescence following emission of an optical phonon by an exciton, are proportional to the square of the nonpolar optical deformation potentials involved, divided by the phonon energy. In the data of Ref. 17, the Γ_{15}^- phonon emission line, which corresponds to the sum of the contributions of two TO (transverse optical) modes and the LO (longitudinal optical) mode, has a maximum intensity about three times higher than the two lower-energy phonon lines, which are roughly equal in maximum efficiency. Using this analysis Snoke *et al.* have fixed the deformation potentials of the Γ_{25}^- and the Γ_{12}^- phonons at 0.72 ± 0.08 times the Γ_{15}^- deformation potential.

The contribution from the optical phonons to the cooling rate per exciton is

$$\begin{aligned} \frac{1}{N} \left(\frac{\partial E}{\partial t} \right)_{\text{opt}} &= - \sum_i \frac{(mv_\gamma^2)^2}{\hbar} \frac{1}{\pi^3} \frac{m}{m_{\text{ion}}} \frac{1}{na^3} \frac{(k_B T)^2 (D_i a)^2}{(\hbar v_\gamma / a)^4} \left(\frac{1}{e^{\beta \hbar \omega_i} - 1} - \frac{1}{e^{\beta \hbar \omega_i} - 1} \right) \\ &\quad \times \int_0^\infty x dx \ln \left(\frac{1 - e^{-w_-}}{1 - e^{-w_+}} \right), \end{aligned} \quad (14)$$

where now the factors v_\pm become $w_\pm \equiv (x \pm \hbar \omega_i / 4k_B T x)^2 - \beta \mu$. The sum is over the group of lower-energy optical phonons. Along the lines of constant α , and small lattice temperature, the cooling rate per particle due to each of the optical phonons varies as $T^{1/2} e^{-\beta \hbar \omega_i / 2}$.

From Eq. (6), the net additional energy loss per condensed exciton, from excited excitons emitting an acoustic phonon and dropping into the condensate is

$$\begin{aligned} \frac{1}{N_{\text{cond}}} \left(\frac{\partial E}{\partial t} \right)_{\text{LA}}^{\text{cond}} &= - \frac{8(mv_\gamma^2)^2}{\pi \hbar} \frac{m}{m_{\text{ion}}} \frac{(mv_\gamma^2) D_a^2}{(\hbar v_\gamma / a)^3} \\ &\quad \times \frac{1}{[1 + (k_0 a / 4)^2]^4} (n_{k_0} - f_{k_0}), \end{aligned} \quad (15)$$

where $k_0 = 2mv_\gamma / \hbar$. For emission of optical phonons,

$$\begin{aligned} \frac{1}{N_{\text{cond}}} \left(\frac{\partial E}{\partial t} \right)_{\text{opt}}^{\text{cond}} &= - \sum_i \frac{(mv_\gamma^2)^2}{2^{1/2} \pi \hbar} \frac{m}{m_{\text{ion}}} \left(\frac{a}{\gamma} \right)^2 \\ &\quad \times \frac{(D_i a)^2 (\hbar \omega_i)^{1/2}}{(mv_\gamma^2)^{3/2} (\hbar v_\gamma / a)^3} (n_{k'_i} - f_{k'_i}), \end{aligned} \quad (16)$$

where $k'_i = (2m\omega_i / \hbar)^{1/2}$.

Combining these various rates, we find the rate of change of the internal energy of the excitons per particle due to the exciton-phonon interaction shown in Figs. 4(a,b) for acoustic and optical phonons, respectively. In these figures the temperatures of the exciton gas and the lattice are kept fixed at 30 K and 6 K, respectively, as the chemical potential and therefore the density is varied. As we see, for typical temperatures and densities, cooling of excitons by acoustic phonons dominates cooling by optical phonons by more than an order of magnitude. Optical phonons do not contribute significantly to the cooling since their energy is greater than that of the majority of the excitons. In contrast, optical phonons play the dominant role in Auger heating, as we discuss in Sec. V, since the process involves either free electrons and holes, or excitons of very large kinetic energies.

The results in Figs. 4(a,b) show a clear effect of degeneracy on the exciton cooling. The rate is constant when the exciton gas is in the classical regime, but it decreases with increasing degeneracy, approaching a lower value as $\alpha \rightarrow 0$. This decrease occurs because energy and momentum conservation limits the number of excitons that are able to interact with phonons as the degeneracy increases. As the gas approaches the condensation phase boundary, the cooling mechanisms become less effective. Furthermore, the dependence of the acoustic-phonon matrix element on momentum transfer [Eq. (10)] enhances this effect. As we discuss in the last section, the smaller cooling rate at high degeneracy plays a significant role in the evolution of the system. A related

classical phenomenon has been observed by Trauernicht and Wolfe²³ in experiments on Cu_2O , where the diffusion constant of paraexcitons shows a sharp rise at low temperatures due to their average velocity falling below the sound velocity.

IV. EXCITON INTERCONVERSION PROCESSES

Orthoexcitons in Cu_2O are observed to convert rapidly to paraexcitons¹² through an acoustic-phonon-assisted process, depicted in Figs. 5(a,b), dependent on temperature but independent of the gas density at low densities.¹¹ At the zone center the orthoexcitons have Γ_{25}^+ symmetry and the paraexcitons Γ_2^+ . Therefore, conversion requires a $\Gamma_{25}^+ \otimes \Gamma_2^+ = \Gamma_{15}^+$ phonon. Since the acoustic phonons at the center of the zone in Cu_2O have Γ_{15}^- symmetry, the matrix element for the conversion process is strongly suppressed. Away from the zone center the matrix element, calculated in the $\mathbf{k} \cdot \mathbf{p}$ approximation, has the form,²⁴

$$|M_c|^2 \sim k_o^2, \quad (17)$$

where k_o is the ortho-exciton wave vector. In this approximation the symmetry of the ortho-exciton wave function is approximately that at the zone center, plus a small component with Γ_{15}^- symmetry of amplitude $\propto k_o$. We begin by calculating the down-conversion rate [Figs. 5(a,b)] when the system is not in the condensed region. We extend the calculation to condensed excitons below.

The down-conversion rate D , is given by

$$\begin{aligned} D &\equiv \frac{1}{N_{o,\text{exc}}} \left(\frac{\partial N_o}{\partial t} \right)_{o \rightarrow p} \\ &= \frac{2\pi}{\hbar} \frac{1}{N_{o,\text{exc}}} \sum_{\mathbf{k}, \mathbf{q}} |M_c|^2 \{ n_{\mathbf{k}}^0 (1 + n_{\mathbf{k}-\mathbf{q}}^p) (1 + f_{\mathbf{q}}) \\ &\quad \times \delta(\varepsilon_{\mathbf{k}} + \Delta - \varepsilon_{\mathbf{k}-\mathbf{q}} - \hbar \omega_{\mathbf{q}}) \\ &\quad + n_{\mathbf{k}-\mathbf{q}}^0 (1 + n_{\mathbf{k}-\mathbf{q}}^p) \delta(\varepsilon_{\mathbf{k}} + \Delta - \varepsilon_{\mathbf{k}-\mathbf{q}} + \hbar \omega_{\mathbf{q}}) \}, \end{aligned} \quad (18)$$

where $N_{o,\text{exc}}$ is the number of noncondensed ortho excitons. We extract the matrix element here from experimental data for down-conversion in the nondegenerate regime,¹² for which the classical limit of Eq. (18) applies. We find for low lattice temperatures that in this limit, $D \approx 0.014 T^{3/2} \text{ ns}^{-1}$ with T measured in kelvin. To determine the rate of energy change rate due to down-conversion we multiply the first term in the summand of Eq. (18) by $(\Delta - \hbar \omega_{\mathbf{q}})$ and the second by $(\Delta + \hbar \omega_{\mathbf{q}})$.

The up-conversion rate U for the processes shown in Figs. 5(c,d) is, similarly,

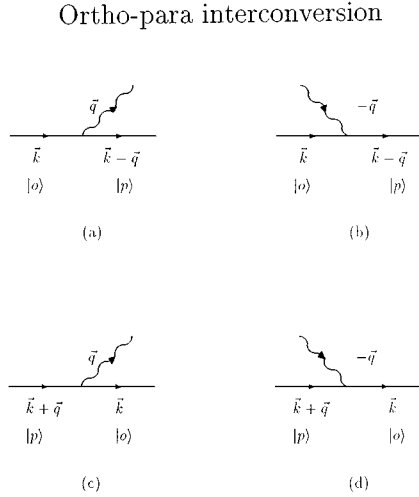


FIG. 5. Ortho-exciton–para-exciton (a,b) down-conversion and para-exciton–ortho-exciton up-conversion (c,d) for acoustic-phonon-mediated mechanisms.

$$\begin{aligned}
 U &\equiv \frac{1}{N_{p,\text{exc}}} \left(\frac{\partial N_p}{\partial t} \right)_{p \rightarrow o} \\
 &= \frac{2\pi}{\hbar} \frac{1}{N_{p,\text{exc}}} \sum_{\mathbf{k}, \mathbf{q}} |M_c|^2 \{ n_{\mathbf{k}+\mathbf{q}}^p (1+n_{\mathbf{k}}^o) (1+f_{\mathbf{q}}) \\
 &\quad \times \delta(\varepsilon_{\mathbf{k}+\Delta} - \varepsilon_{\mathbf{k}-\mathbf{q}} + \hbar\omega_{\mathbf{q}}) \\
 &\quad + n_{\mathbf{k}+\mathbf{q}}^p f_{-\mathbf{q}} (1+n_{\mathbf{k}}^o) \delta(\varepsilon_{\mathbf{k}+\Delta} - \varepsilon_{\mathbf{k}-\mathbf{q}} - \hbar\omega_{\mathbf{q}}) \}, \quad (19)
 \end{aligned}$$

where $N_{p,\text{exc}}$ is the number of noncondensed para excitons. Since the ortho-para energy splitting $\Delta E = 12$ meV is $\gg k_B T$ for temperatures of interest, U is much smaller than D . To determine the rate of energy change due to this process we multiply the first term of the summand of Eq. (19) by $-(\Delta + \hbar\omega_{\mathbf{q}})$ and the second by $(-\Delta + \hbar\omega_{\mathbf{q}})$.

We turn now to the condensed excitons. Equation (17) implies that down-conversion of condensed ortho excitons ($k_o = 0$) is suppressed by the symmetry of the excitons and the phonons at the center of the zone of Cu_2O . The up-conversion of condensed paraexcitons is not possible either, because energy and momentum cannot be conserved for the parameters of Cu_2O . Thus only excitons in *excited* states participate in this mechanism. The conversion process primarily influences the ortho excitons, since the up-conversion rate of para excitons is small. Condensation of ortho excitons would in fact help them to maintain their high density and lower the heating by down-conversion.

Figure 6 shows the calculated rates of the down- and up-conversion processes as a function of temperature at fixed α . As expected both the down-conversion and the up-conversion rates increase with exciton temperature. On the other hand, both rates are suppressed as the degeneracy increases.

V. AUGER PROCESS

The nonradiative direct and phonon-assisted Auger decay processes, illustrated in Figs. 7 and 8, are the most important

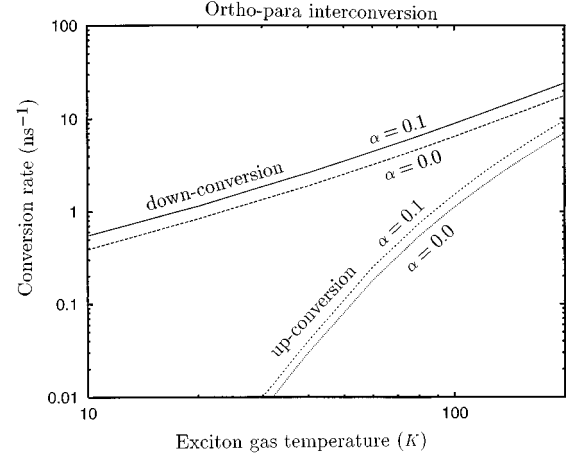


FIG. 6. The down-conversion and up-conversion rates are shown for $\alpha_o = \alpha_p = 0$ and $\alpha_o = \alpha_p = 0.1$ as a function of the temperature of the exciton gas.

mechanisms for loss of excitons at high densities. Studies of this mechanism have been carried out on excitons in Cu_2O ,^{9,13} and in electron-hole plasmas^{25,26} where an electron recombines and excites either another electron high in the conduction band, or a hole deep in the valence band. Detailed calculations of the Auger rates are given in Ref. 9; we summarize the results here.

The band structure of the material plays an essential role in the Auger annihilation of excitons. Because the conduction and the valence bands have the same (even) parity,²⁷ the rate of the direct Auger process (Fig. 7) without Umklapp is negligible, and the Umklapp terms are small. Although the phonon-assisted Auger process (Fig. 8) is suppressed by the

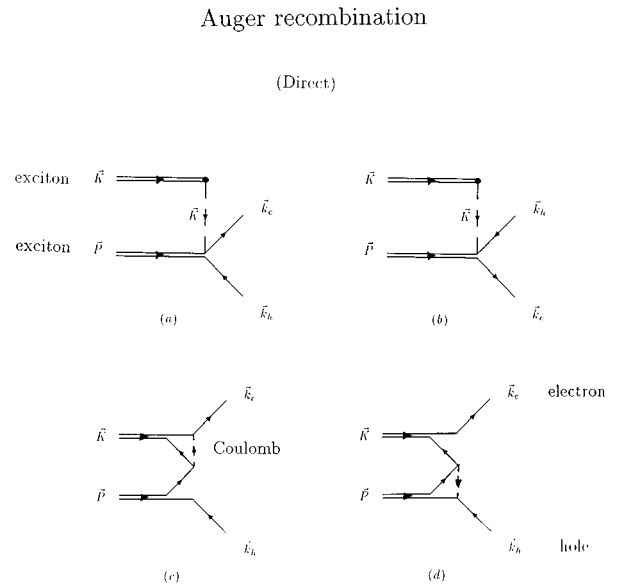


FIG. 7. Direct Auger nonradiative annihilation processes. Time progresses from left to right. The initial state contains two excitons of momenta \mathbf{K} and \mathbf{P} , and the final state contains an ionized electron and hole with momenta \mathbf{k}_e and \mathbf{k}_h , respectively. The dashed line denotes the Coulomb interaction.

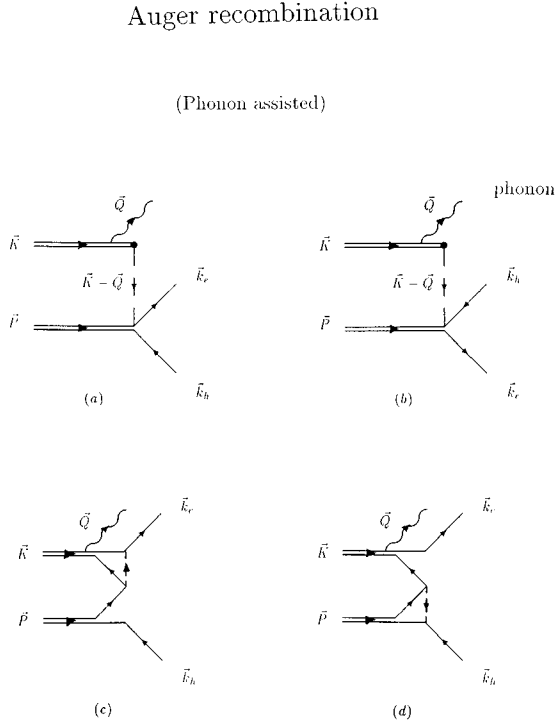


FIG. 8. Phonon-assisted Auger nonradiative annihilation processes. The wiggly line denotes a phonon of momentum \mathbf{Q} .

additional matrix element for phonon emission, the process is dominated by a large non-Umklapp term when the phonon has negative parity. The process is in fact faster than the direct. The rate of phonon-mediated para-para Auger annihilations is negligible compared with the rates for ortho-ortho and ortho-para; the reason is that the intermediate negative-parity band which enters the process is very close in energy to the conduction band for the ortho-exciton recombination vertex entering ortho-ortho or ortho-para collisions, but it is a deep valence band for the paraexciton vertex entering para-para collisions.

The Auger decay times appearing in Eqs. (2) and (3) are given by⁹

$$\frac{1}{\tau_{Ao}^{\text{ph}}} = \frac{C}{2} \left(n_o + \frac{1}{2} n_p \right), \quad (20)$$

$$\frac{1}{\tau_{Ap}^{\text{ph}}} = \frac{C}{4} n_o, \quad (21)$$

for the phonon-assisted process, where the constant C is of order 0.4 ns^{-1} , when the exciton densities n_i are measured in units of 10^{18} cm^{-3} . The Auger decay rate depends only on the density of excitons for low lattice temperatures. Since the Auger matrix element is constant when the thermal energy of excitons (a few meV) is much less than the gap energy E_g ($=2.17 \text{ eV}$ in Cu_2O), the decay rate depends on neither the exciton temperature nor the statistics. Auger collisions are not influenced by the thermal motion of the excitons, and, hence, the decay rate is the same for degenerate and classical gases of the same density.

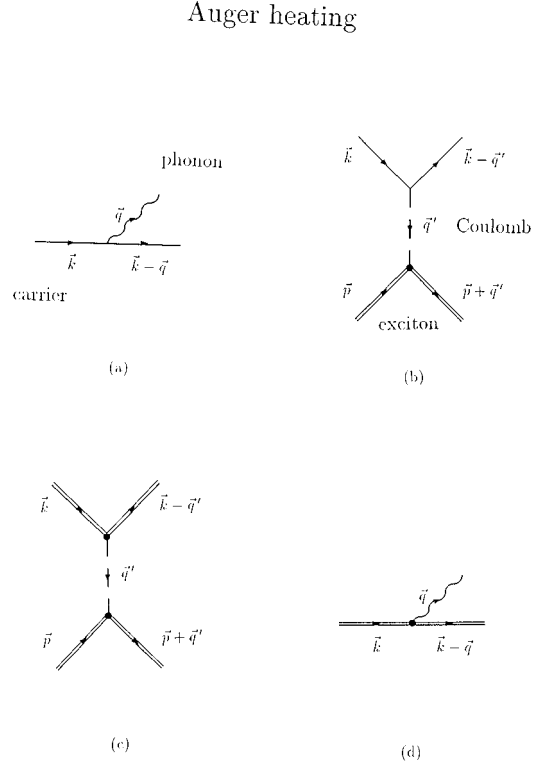


FIG. 9. Energy transfer processes among hot electrons and holes (single lines), excitons (double lines), and phonons (wiggly lines). (a) and (b) describe (Auger or laser-generated) electron (hole) phonon and electron (hole) exciton scattering processes, respectively; (c) hot exciton-thermalized exciton scattering; (d) hot exciton-phonon scattering.

The Auger process produces hot carriers within the exciton gas — ionized electrons and holes — excited by an energy of the order of the energy gap. The hot carriers primarily lose this energy by emission of a cascade of phonons [Fig. 9(a)] — and to a lesser extent by scattering with excitons [Fig. 9(b)] — and eventually reform excitons.²⁸ To calculate the fraction of Auger energy that heats the exciton gas we split the problem into two parts, before and after the exciton is formed. We shall see that only a small fraction of the hot-carrier energy goes into heating the gas, because the carriers are quickly cooled by rapid Fröhlich emission of optical phonons. In contrast, the hot excitons have a slower phonon emission rate, and their kinetic energy is more readily shared with the thermalized excitons.

The cooling of the carriers by optical phonon emission [Fig. 9(a)] is given by

$$\left(\frac{\partial E_{\mathbf{k}}}{\partial t} \right)_{\text{opt}} = - \frac{2\pi}{\hbar} \sum_{\mathbf{q}} |M_{\mathbf{q}}|^2 \hbar \omega_i \delta(E_{\mathbf{k}} - E_{\mathbf{k}-\mathbf{q}} - \hbar \omega_i). \quad (22)$$

At high energies the Fröhlich polar interaction¹⁶ is the dominant process for the emission and absorption of free carriers by optical phonons. If there is only one optical phonon branch, the matrix element for the Fröhlich interaction is

$$|M_{\mathbf{q}}|^2 = \frac{2\pi e^2}{V} \left(\frac{1}{\epsilon_\infty} - \frac{1}{\epsilon_0} \right) \frac{\hbar \omega_i}{q^2}. \quad (23)$$

Here $\epsilon_\infty = 6.46$ is the high frequency and $\epsilon_0 (= 7.11)$ is the static dielectric constant; these two dielectric constants differ only slightly as a consequence of Cu_2O being almost nonpolar.¹⁹ Since Cu_2O has a large number of optical phonon modes, Eq. (23) can only be applied approximately; for the lowest optical phonon of energy 11.4 meV, it leads to a rate ~ 50 eV/ns for the highest energy of the carriers (≈ 1 eV); the net rate should be even higher.

The rate of energy change of a hot carrier of momentum \mathbf{k} and energy $E_{\mathbf{k}}$ due to collisions with thermalized excitons of momentum \mathbf{p} and energy $\epsilon_{\mathbf{p}}$ [Fig. 9(b)] is given by

$$\left(\frac{\partial E_{\mathbf{k}}}{\partial t} \right)_{\text{exc}} = - \frac{2\pi}{\hbar} \sum_{\mathbf{p}, \mathbf{q}} |M_{\mathbf{q}}^{\text{ce}}|^2 n_{\mathbf{p}} (1 + n_{\mathbf{p}+\mathbf{q}}) (E_{\mathbf{k}} - E_{\mathbf{k}-\mathbf{q}}) \times \delta(\epsilon_{\mathbf{p}+\mathbf{q}} + E_{\mathbf{k}-\mathbf{q}} - \epsilon_{\mathbf{p}} - E_{\mathbf{k}}), \quad (24)$$

where $M_{\mathbf{q}}^{\text{ce}}$ is the carrier-exciton matrix element. If we assume a momentum transfer $q \gg p$, then

$$\left(\frac{\partial E_{\mathbf{k}}}{\partial t} \right)_{\text{exc}} \approx - \frac{2\pi}{\hbar} \sum_{\mathbf{p}} n_{\mathbf{p}} \sum_{\mathbf{q}} |M_{\mathbf{q}}^{\text{ce}}|^2 \epsilon_{\mathbf{q}} \delta(\epsilon_{\mathbf{q}} + E_{\mathbf{k}-\mathbf{q}} - E_{\mathbf{k}}). \quad (25)$$

As we derive in the Appendix, the matrix element $M_{\mathbf{q}}^{\text{ce}}$ is

$$M_{\mathbf{q}}^{\text{ce}} \approx \frac{2\pi e^2 a^2}{\epsilon_0 V} \frac{(\lambda_e - \lambda_h)}{[1 + (qa/4)^2]^3}, \quad (26)$$

where $\lambda_e = m_e/m = 0.58$ and $\lambda_h = m_h/m = 0.42$. (As mentioned earlier the exciton mass is not equal to the sum of the effective electron and hole masses; we assume, however, that the ratios m_e/m and m_h/m are the same as those following from the assumption $m = m_e + m_h$.) This process gives a cooling rate ~ 1 eV/ns, some 2% of the lowest optical phonon cooling rate, Eq. (22). Furthermore, the ratio of the rates of carrier-exciton to phonon cooling decreases with decreasing carrier energy.

When the hot carriers lose sufficient energy they reform hot excitons, which heat the exciton gas by scattering with thermal excitons. It is this heating of the exciton gas that stands in the way of the excitons crossing the phase boundary into the condensed region. Cooling of hot excitons by phonon emission is competitive, but does not heat the exciton gas. Heating of the excitons per Auger pair recombination is, at most, of the order of the exciton binding energy. To calculate the kinetic energy transferred to the exciton gas by this Auger annihilation process, we note that the newly formed excitons scatter against the thermalized excitons [Fig. 9(c)] and cool at a rate

$$\left(\frac{\partial \epsilon_h}{\partial t} \right)_{\text{exc}} = - \frac{\epsilon_h}{2} n v_{\text{rel}} \sigma(v_{\text{rel}}) \equiv - \frac{\epsilon_h}{2\tau_{\text{sc}}}, \quad (27)$$

where ϵ_h is the kinetic energy of a hot exciton, $\sigma(v_{\text{rel}})$ the exciton-exciton scattering cross section, v_{rel} the relative velocity of the excitons, and n the thermalized exciton density. At low energy the cross section is $\sigma(v_{\text{rel}}) = 4\pi(2a_{\text{sc}})^2$, with a single-exciton radius for exciton-exciton collisions, a_{sc} .

We use $a_{\text{sc}} = 3.0 \text{ \AA}$, which approximates the numerically calculated interaction potential²⁹ quite well. At high energy the cross section calculated in Born approximation taking into account Coulomb interactions between the electrons and holes in the different excitons is

$$\sigma(v_{\text{rel}}) = \frac{33}{35} \pi a^2 \left(\frac{e^2}{\hbar v_{\text{rel}} \epsilon_0} \right)^2. \quad (28)$$

A simple interpolation between these limits is

$$\sigma(v_{\text{rel}}) = \frac{4\pi(2a_{\text{sc}})^2}{1 + (140/33)(k_{\text{rel}} a_{\text{sc}})^2}, \quad (29)$$

where $k_{\text{rel}} = (m v_{\text{rel}}/\hbar)$. In the limit that the hot exciton energy is much larger than that of the thermalized excitons, Eqs. (27)–(29) give

$$\left(\frac{\partial \epsilon_h}{\partial t} \right)_{\text{exc}} = - \hbar \omega_i^2 \left(\frac{a_{\text{sc}}}{a} \right)^2 n a^3 \frac{2^{7/2} \epsilon_h^{3/2}}{(\hbar \omega_i)^2} \left(\frac{\hbar^2}{m a^2} \right)^{1/2} \times \frac{1}{(1 + (280/33) m a_{\text{sc}}^2 \epsilon_h / \hbar^2)}. \quad (30)$$

The prefactor $\hbar \omega_i^2$ is ≈ 198 eV/ns for the lowest-energy optical phonon of 11.4 meV.

Hot excitons also cool by phonon emission [Fig. 9(d)] without heating the exciton gas. The rate of cooling of a hot exciton of momentum \mathbf{k} and energy $\epsilon_{\mathbf{k}}$ by optical phonon emission is given by

$$\left(\frac{\partial \epsilon_{\mathbf{k}}}{\partial t} \right)_{\text{opt}} = - \frac{2\pi}{\hbar} \sum_{\mathbf{q}} |M_{\mathbf{q}}^{\text{opt}}|^2 \hbar \omega_i \delta(\epsilon_{\mathbf{k}} - \epsilon_{\mathbf{k}-\mathbf{q}} - \hbar \omega_i), \quad (31)$$

with squared matrix element (13). Emission of optical phonons via deformation potential coupling cools a hot exciton of kinetic energy $\epsilon_h > \hbar \omega_i$ at a rate

$$\left(\frac{\partial \epsilon_h}{\partial t} \right)_{\text{opt}} = - \sum_i \hbar \omega_i^2 \left(\frac{\epsilon_h}{\hbar \omega_i} - 1 \right)^{1/2} \times \frac{m}{m_{\text{ion}}} \left(\frac{a_{\text{c}}}{a} \right)^2 \frac{(D_o a)^2 \epsilon_h^{1/2}}{2^{1/2} \pi (\hbar \omega_i)^{3/2}} \left(\frac{\hbar^2}{m a^2} \right)^{1/2}. \quad (32)$$

For hot excitons, all 15 optical phonon modes need to be taken into account in the sum. The measurements of Snoke *et al.* probe only the three lowest optical phonons Γ_{25}^- , Γ_{12}^- , and Γ_{15}^- , of energies 11.4, 13.8, and 18.7 meV, respectively. For the Γ_{12}^- optical phonon of 13.8 meV, for example,

$$\left(\frac{\partial \epsilon_h}{\partial t} \right)_{\Gamma_{12}^-} \approx -0.16 \left(\frac{\epsilon_h}{\hbar \omega_{\Gamma_{12}^-}} - 1 \right)^{1/2} \text{ eV/ns}. \quad (33)$$

In addition, excitons of energy higher than $2\hbar \omega_i$ can cool by a fast parity-conserving two optical-phonon emission process.¹⁸ For the simultaneous emission of two Γ_{12}^- phonons of 27.6 meV, Snoke *et al.* have placed experimental limits on the cooling rate which indicate that it is at least ten times larger than the single-phonon rate. They have also found that the two- Γ_{25}^- -phonon cooling mechanism is too small to be observed. The complete treatment of optical-phonon cooling

including all phonon processes is beyond the scope of our present study and indeed requires much more experimental input. Nevertheless, we can use the experimentally derived exciton cooling rates of Snoke *et al.* involving the three lowest optical-phonon branches as a gauge of the total cooling rate for all optical-phonon processes. We introduce the cooling parameter $\gamma (> 1)$ such that

$$\left(\frac{\partial \epsilon_h}{\partial t}\right)_{\text{opt}}^{\text{tot}} = \gamma \left[\left(\frac{\partial \epsilon_h}{\partial t}\right)_{\Gamma_{12}^-} + \left(\frac{\partial \epsilon_h}{\partial t}\right)_{2\Gamma_{12}^-} \right]. \quad (34)$$

We shall see that a fit of the short-pulse experimental results yields $\gamma \approx 4.5$.

At energies lower than the lowest optical phonon energy only acoustic phonons can be emitted; the cooling rate for coupling to longitudinal acoustic phonons calculated with a deformation potential coupling is

$$\begin{aligned} \left(\frac{\partial \epsilon_h}{\partial t}\right)_{\text{LA}} &= -\hbar \omega_i^2 \frac{m}{m_{\text{ion}}} \left(\frac{a'}{a}\right)^4 \frac{2^{7/2} D_a^2}{3\pi (\hbar \omega_i)^2 \epsilon_h^{1/2}} \\ &\times \left(\frac{\hbar^2}{ma'^2}\right)^{1/2} \frac{z_0^2 (z_0 + 3)}{(1 + z_0)^3}, \end{aligned} \quad (35)$$

where $z_0 = 2[(2m\epsilon_h a^2)^{1/2} - (mv/a)/\hbar]$. In general the exciton-phonon interaction is not as effective at cooling excitons as it is as for free carriers. For the polar interaction this is due to the electrical neutrality of the exciton and for the deformation potential scattering the matrix element of the process involves the difference of the deformation potentials for the conduction and the valence bands.

The total cooling rate of a hot exciton due to phonon emission and scattering with thermalized excitons is

$$\frac{d\epsilon_h}{dt} = \left(\frac{\partial \epsilon_h}{\partial t}\right)_{\text{ph}} + \left(\frac{\partial \epsilon_h}{\partial t}\right)_{\text{exc}}, \quad (36)$$

where $(\partial \epsilon_h / \partial t)_{\text{ph}}$ is the total phonon cooling rate of hot excitons, the sum of Eqs. (34) and (35). The heat transferred to the exciton gas, E_A , per Auger annihilation process is then

$$E_A = - \int_0^{t_0} dt \left(\frac{\partial \epsilon_h}{\partial t}\right)_{\text{exc}}, \quad (37)$$

where t_0 is the time it takes for the hot exciton to fall to the mean kinetic energy of a thermalized exciton. This time must be found numerically by solving for the time evolution of the kinetic energy of the hot exciton.

We note that Auger heating depends strongly on the exciton density; it depends only weakly on the exciton temperature because the higher the kinetic energy of the exciton gas, the less energy is transferred from hot to cold excitons. Auger heating does not depend on the degeneracy of the gas. In the limit that the density of the thermalized excitons goes to zero, the Auger heating goes to zero. In the limit that the exciton density is very large, the Auger heating is equal to the binding energy E_b , since all the energy goes to the excitons. The ratio E_A/E_b as a function of the density of the thermalized excitons is shown in Fig. 10, assuming that the exciton gas temperature is kept fixed at $T=30$ K.

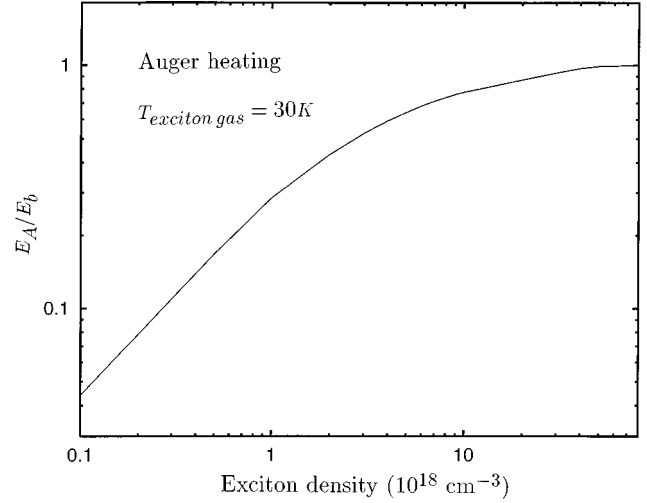


FIG. 10. The ratio of the Auger heating E_A over the binding energy E_b versus the density of the thermalized excitons, at fixed exciton temperature 30 K.

The rate of energy change of the exciton gas due to Auger heating is

$$\frac{1}{N} \left(\frac{\partial E}{\partial t}\right)_A = \frac{E_A}{\tau_A^{\text{ph}}}, \quad (38)$$

where $(\tau_A^{\text{ph}})^{-1} \equiv -(1/N)(\partial N / \partial t)_A = (C/4)n_o$ is the total Auger scattering rate for the excitons, Eqs. (20) and (21). Since the laser creates ionized electrons and holes with an excess kinetic energy of about 250 meV per pair, an energy larger than E_b , the heating of the exciton gas from hot carriers generated by the laser is the same as the Auger heating E_A . The rate at which the laser heats the excitons is effectively E_A times the laser production rate, and for a given density and temperature of the exciton gas the total heating rate due to Auger decay and the laser production is E_A times the sum of the Auger rate and the laser generation rate.

VI. RESULTS

In the previous sections we have derived from experimental measurements and theoretical considerations numerical values of the parameters entering the rates of energy change of the exciton gas due to phonon cooling, the rates of ortho-para interconversion and energy exchange, and the Auger decay rate. The processes of Auger and laser heating involve the uncertain cooling parameter γ , Eq. (34). We now solve the kinetic equations (2)–(4) for $N_o(t)$, $N_p(t)$, and $T(t)$ numerically, assuming reasonable initial conditions for these quantities at $t=0$. We choose γ to optimize agreement between our results and the experimental data, for the case of short-pulse excitation, (Sec. VI A; Fig. 11) and keep this parameter fixed in the rest of our calculation. We find that $\gamma \approx 4.5$, a reasonable number as an average of the cooling rate of a hot exciton due to all the optical phonons of Cu_2O (including single and multiple-phonon processes) in terms of the Γ_{12}^- plus $2\Gamma_{12}^-$ optical-phonon cooling rate.

In the present calculations of the dynamics we assume that the orthoexcitons are triply degenerate and, hence, we

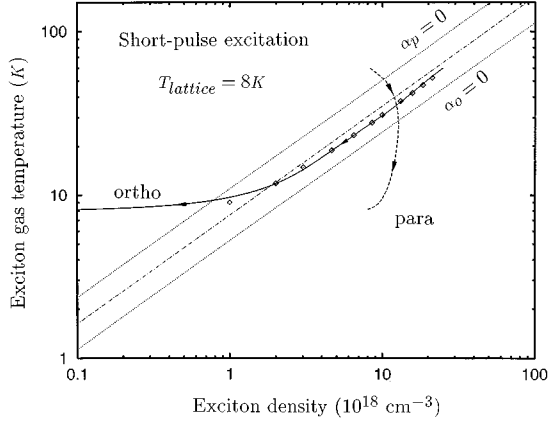


FIG. 11. Numerical solution of Eqs. (2)–(4) in the density-temperature plane for the ortho excitons (solid line) and para excitons (dashed line), for a short laser pulse. The diamonds are (long-pulse) experimental data for ortho excitons. The two dotted lines are Bose-Einstein condensation boundaries for ortho excitons (lower) and para excitons (higher). The dash-dot line shows the adiabat of stability [see Eq. (41)] with only acoustic-phonon-cooling and Auger heating taken into account.

compare our orthoexciton calculations with the zero-stress data. No experimental determination of the para exciton density has been made in the zero-stress case. We find, however, that predictions for the para excitons at zero stress agree remarkably well with the observed para-exciton behavior under stress. This is not surprising as the paraexciton multiplicity does not change with applied stress.

The numerical simulations together with the argument, given in the Introduction, that the orthoexcitons should approach an adiabat just above the condensation line, put us in a position to identify the crucial factors that lead to the quantum saturation of ortho excitons, while allowing condensation of para excitons. At the outset, we note that no single process we consider poses an obviously insurmountable barrier to Bose-Einstein condensation. To show in detail the physical effects of the various processes we take the approach of first computing the behavior of the gas with all the known factors in the equations, and then dissecting the problem by removing each of the processes from the calculation in turn.

A. “Short-pulse” excitation

A mode-locked, cavity-dumped argon-ion laser produces nanjoule pulses with about a 100 ps length. For the photoluminescence time resolution of about 100 to 300 ps, this excitation pulse is effectively a δ function in time, and the evolution of the system is observed without creation by the laser of further particles. The excitons, whose energy relaxation and decay we are dealing with, form on a time scale shorter than the detection limits; as we shall see, most of the action occurs within a few nanoseconds. We compute the behavior of both ortho excitons and para excitons in this “short-pulse” case, even though the radiative efficiency of the para excitons is a factor 500 less than that of the (higher-energy) ortho excitons, making it difficult to observe the para excitons during this short time period.

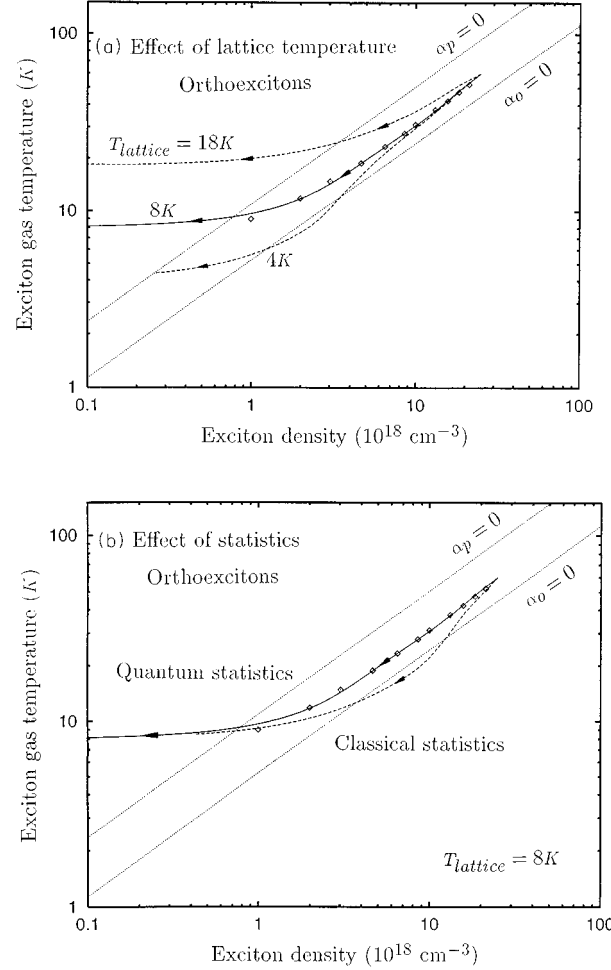


FIG. 12. (a) Calculated behavior of ortho excitons for three different lattice temperatures, 18 K (higher), 8 K (middle), and 4 K (lower), assuming a short laser pulse. (b) Behavior of ortho excitons assuming classical and degenerate statistics for the exciton-phonon interaction.

Figure 11 shows the result of our simulation with initial conditions, $n_o = 25 \times 10^{18} \text{ cm}^{-3}$ and $n_p = 8.33 \times 10^{18} \text{ cm}^{-3}$ at a temperature of 60 K, and T_ℓ fixed at 8 K. We assume in this and the long-pulse case that the laser produces three ortho excitons for each para exciton, as discussed earlier. For comparison to experiment in this figure and those that follow, we plot Snoke’s ortho-exciton data (diamonds) for the long-pulse case between $n_o = 10^{18} \text{ cm}^{-3}$ and $2 \times 10^{19} \text{ cm}^{-3}$. The solid and dashed curves represent the theoretical ortho exciton and para exciton trajectories, respectively, over the time $t=0$ to 2 ns. As time progresses the excitons cool. The dotted straight lines are the Bose-Einstein condensation lines, the upper for para excitons ($g = 1$) and the lower for ortho excitons ($g = 3$).

A principal result of our study is that, as in experiment, the ortho excitons move closely parallel to the phase boundary without crossing it, following an adiabat, as a result of the balance between the phonon cooling and the Auger heating, Eq. (1). We present the details of this argument in Sec. VI C. When the ortho-exciton density falls sufficiently low ($< 10^{18} \text{ cm}^{-3}$), and their temperature approaches that of the lattice, the ortho excitons move away from the condensation

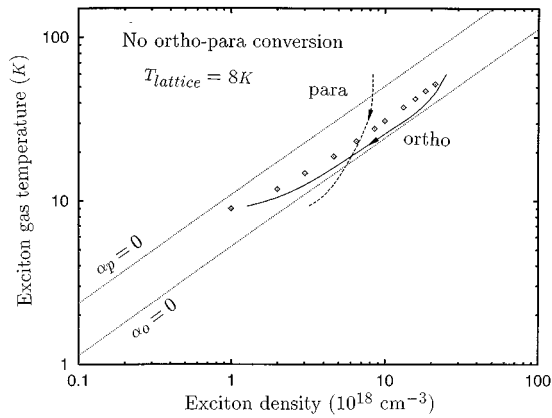


FIG. 13. Short laser-pulse excitation. No ortho-para interconversion process.

line; their density continues to decrease due to ortho-to-para conversion and Auger recombination.

The calculations further predict that the para excitons quickly cool below their phase boundary and condense. There is little decay in the density of the para excitons over the 2-ns time interval; in fact, their density initially increases due to the down-conversion of ortho excitons. Once the ortho excitons are gone, the para excitons decay on a scale of their recombination time, which is longer than the chosen time interval. Note that the two components cover the same temperature range because we have assumed, as throughout, that they are in good thermal contact with each other and thus have the same temperature.

Now let us examine how changing specific quantities in our calculation changes the results, starting with the lattice temperature. We expect that at lower lattice temperatures, the ortho excitons cool more efficiently. We see from Fig. 12(a) that this is true to a small extent. With a lattice temperature of 4 K, the ortho excitons still follow the same trajectory at high density — implying that the heating is associated with other processes — but as the gas density reduces below about $3 \times 10^{18} \text{ cm}^{-3}$ a brief crossing of the phase boundary occurs. Unfortunately, there is no direct experimental control over the local lattice temperature: the bath temperature is already 2 K and the rise in lattice temperature is indirectly caused by the phonon emission of photoexcited carriers. Matters could be worse: we see in the figure that a lattice temperature of 18 K makes Bose-Einstein condensation highly improbable for the ortho excitons.

The assumption of quantum statistics in the exciton-phonon cooling processes has a marked effect on the quantum saturation, as shown in Fig. 12(b). Taking classical statistics (hypothetically) in the cooling process, we see that the orthoexciton gas does not follow a constant- α trajectory at any stage. The quantum effects shown in Fig. 4 — reductions in the cooling rates at high quantum degeneracy — apparently have a deleterious effect on the condensation.

Now let us restore the quantum statistics and observe the effect turning off ortho-to-para conversion. As we see in Fig. 13 the para excitons, while still predicted to condense, do not show an increase in density with time, because one source of para excitons has been removed. Still, Auger recombination diminishes the density of both types of particles. The ortho

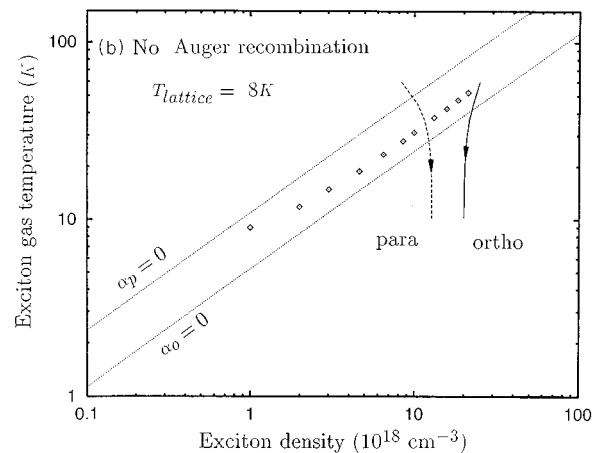
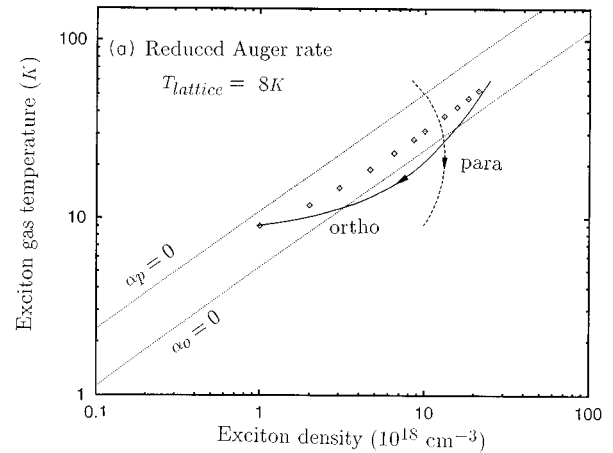


FIG. 14. Short laser-pulse excitation. (a) Auger rate reduced by 50%; (b) Auger process turned off.

excitons, however, come considerably closer to their phase boundary because one of their decay mechanisms has been deleted. Yet, no condensation is predicted for the ortho excitons. Ortho-to-para conversion is not the dominant culprit in preventing their condensation.

Next let us see how the Auger recombination process affects the system. In the calculation shown in Fig. 14(a) we assume that the Auger rate (and, therefore, the Auger heating) is reduced by 50%. This decrease enhances the density of both species at a given time and lowers the temperature of the exciton gas. We see that the ortho excitons are barely able to condense in this case. To carry this effect to the extreme we remove the Auger recombination completely, with the result shown in Fig. 14(b). In this case the total number of excitons is nearly conserved on the 2-ns time scale because the radiative lifetimes of the excitons are much longer. Ortho-to-para conversion causes the density changes seen in the figure. The condensation of both the ortho excitons and para excitons is now unavoidable. Actually, there are two reasons for this: first, the decay of both species is reduced, and, second, there is no Auger heating, which depends strongly on the exciton density and pushes the excitons away from the phase boundary.

Optimistically, we can say that Nature has been kind. Were the Auger rate 50% larger, it is unlikely that even the

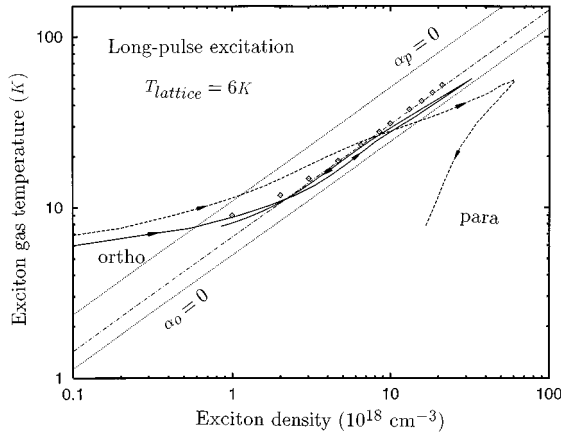


FIG. 15. The behavior of ortho excitons and para excitons in the density-temperature plane, for a long (10-ns) laser pulse. The dash-dot line shows the adiabat of stability [see Eq. (41)] with only acoustic-phonon cooling and Auger heating taken into account.

quantum saturation effect — which, as we have seen here, indeed senses the quantum statistics — would be observable.

B. “Long-pulse” excitation

If the mode locker is removed from the laser, the cavity-dumped mode provides 10-ns-long pulses with about an order of magnitude more energy. Now we must incorporate the generation rate of the laser in the numerical calculation. We assume that the initial temperature of the exciton gas is equal to the lattice temperature, which we take to be 6 K. To start the gas off in the classical regime, we choose initial densities of $0.1 \times 10^{18} \text{ cm}^{-3}$ for the ortho excitons and $0.033 \times 10^{18} \text{ cm}^{-3}$ for the para excitons. We further assume that the temporal laser profile is Gaussian and as before that three ortho excitons are produced for each para exciton.

The principal result of our calculation is shown in Fig. 15. Now the ortho excitons initially move up the phase boundary, towards higher density and temperature, and decay closely along the same path. This is precisely the remarkable quantum-saturation behavior which we hoped to reproduce theoretically and understand. In addition, we see that the para excitons heat up with the ortho excitons, but they are able to cross their phase boundary at an early stage, implying that the gas has a condensed fraction. At the peak of the laser pulse, both ortho-exciton and para-exciton densities begin to decrease. The para-excitons retain a high density as they cool and eventually reach a condensed fraction of over 90%! The numerical simulation is remarkably similar to the data of Lin and Wolfe⁷ in their uniaxially stressed sample. As previously stated, we do not expect major changes in the calculated behavior for the stressed and unstressed cases.

For clarity, we reproduce in Figs. 16 the results of Fig. 15, showing separately the build-up and decay processes. In our calculation, a pulse with a full width at half maximum of 3 ns is used, as shown in the insets of Figs. 16. Figure 16(a) plots the (upwardly rising) gas trajectories for the first half of the laser pulse, and Fig. 16(b) shows the (downward falling) results for the second half of the laser pulse. We note that the initial conditions of the “decay phase” differ from those of the short-pulse experiments: here, the “initial” para-exciton

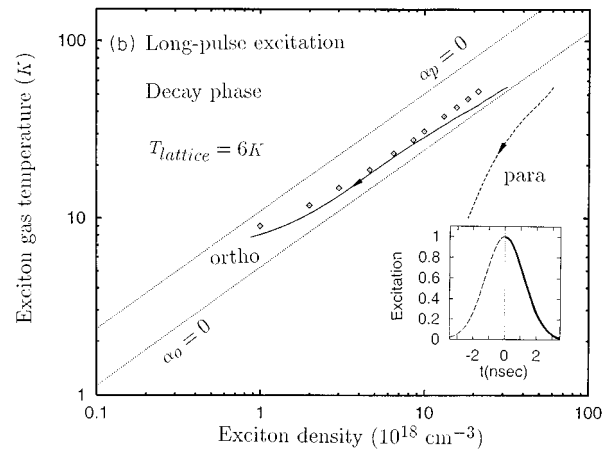
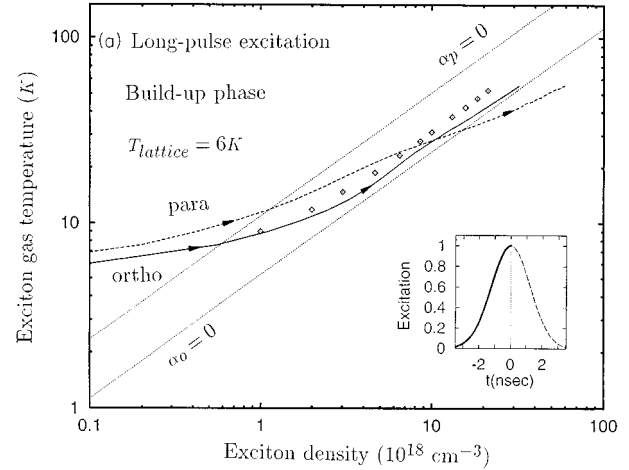


FIG. 16. The buildup (a) and decay (b) phases of Fig. 15.

density is considerably higher than the ortho-exciton density, because the ortho-to-para conversion process has had the entire first half of the laser pulse to pump up the para-exciton density.

Again, we test the effect of quantum statistics in the phonon cooling processes. Figure 17 shows that in the case of

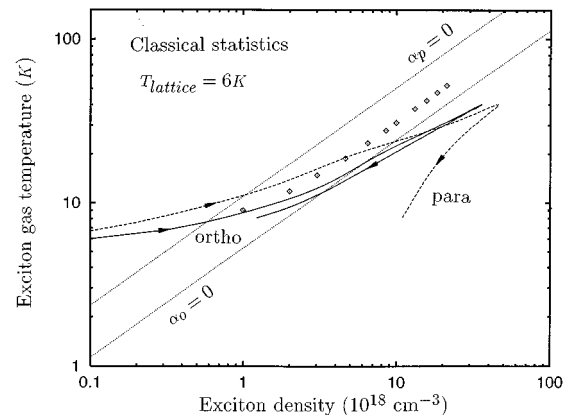


FIG. 17. Behavior of ortho excitons and para excitons assuming classical statistics for the exciton-phonon interaction, for long laser-pulse excitation.

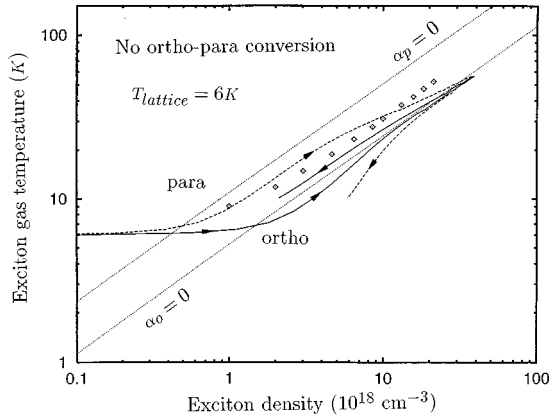


FIG. 18. Behavior of ortho excitons and para excitons in the density-temperature plane, ignoring the interconversion process, for long laser-pulse excitation.

“classical” phonon cooling, both ortho excitons and para excitons are predicted to condense. Thus, the quantum statistics play a crucial role in keeping the ortho excitons away from the condensed region.

In Fig. 18 we show the result of our calculation if we neglect the ortho-para interconversion mechanism. As seen from this figure, the ortho excitons condense, but still tend to move along the condensation line. A major difference between this graph and the data shown in Fig. 2(b) is the faster decay rate here of the para excitons at late times. The reason for this is the lack of the ortho-to-para conversion mechanism, which balances the loss of para excitons due to the Auger process.

In Fig. 19 we show the result of our calculation if the Auger process (annihilation and heating) is neglected. Both species condense for the same reasons as those given for the short-pulse excitation, in Fig. 14(b). The effect of the Auger heating itself (with unmodified Auger annihilation) is shown in Figs. 20(a,b), where we assume that the scattering radius a_{sc} for carrier-carrier scattering is ten times smaller or larger, respectively, than assumed in Fig. 15. This scattering length influences the kinetic energy transferred from the Auger-ionized carriers to the thermalized excitons. In the first case

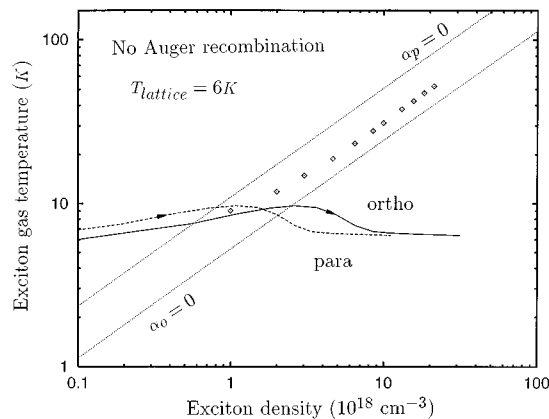


FIG. 19. Behavior of ortho excitons and para excitons in the density-temperature plane, ignoring the Auger (heating and decay) process, for long laser-pulse excitation.

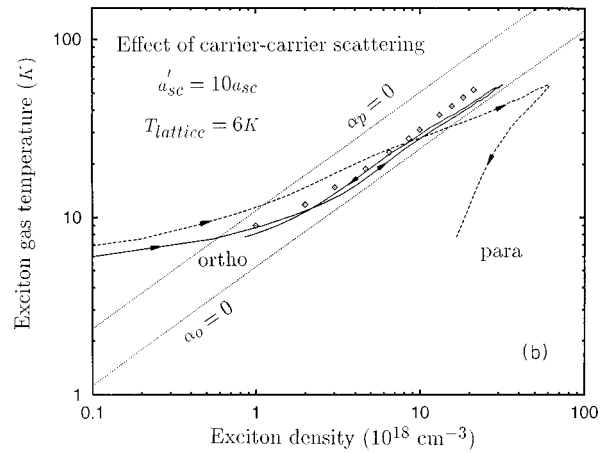
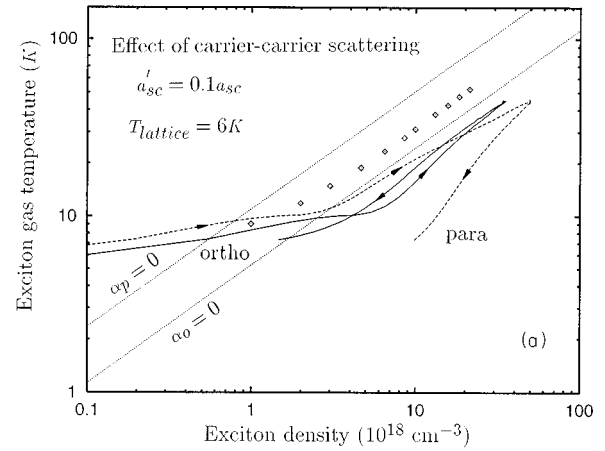


FIG. 20. Behavior of ortho excitons and para excitons in the density-temperature plane, for long laser-pulse excitation, assuming that the scattering radius for exciton-exciton collisions (a) reduced by a factor of ten, and (b) ten times larger than in Fig. 15.

both species condense because of the low Auger heating. In the second case, however, the behavior of excitons hardly changes from that of the initial calculation, Fig. 15. The reason for this is that, according to Eq. (29), the cross section for the scattering is independent of the exciton radius at large radius, and in this limit the rate of energy transfer is dominated by the scattering process.

Finally, in Fig. 21 we investigate the result of changing the Auger decay constant C and the acoustic-phonon deformation potential D_a . The constant C determines the Auger decay rate and consequently the Auger heating rate. Also D_a determines the dominant phonon cooling rate, which is the acoustic-phonon mechanism. For values of C and D_a inside the shaded region, the ortho excitons move along and closely to the condensation line, i.e., between the two critical lines for condensation of the ortho excitons and the para excitons. The region corresponds to $0 \leq \alpha_0 \leq 0.45$. For values of C and D_a above the shaded region, the ortho excitons condense because of the more effective phonon cooling, the low Auger decay rate and the low Auger heating. Below the shaded region the ortho excitons move away from the degenerate regime, towards the classical regime, because of the low phonon-cooling rate, the high Auger decay rate, and the high Auger heating.

C. Entropy of ortho excitons

In the Introduction we briefly outlined the argument that the balance between the rates of phonon cooling and Auger heating causes the ortho excitons to approach a critical adiabat, a line of constant entropy per particle of the ortho excitons, s_o , lying slightly above the condensation phase boundary. We now spell out the calculation in detail. The rate of change of s_o is given by

$$T \frac{ds_o}{dt} = \frac{1}{N_o} \frac{dE_o}{dt} - \frac{Ts_o + \mu_o}{N_o} \frac{dN_o}{dt} + \frac{P_o}{N_o} \frac{dV}{dt}, \quad (39)$$

where E_o is the total energy and P_o the pressure of the ortho-exciton gas.

The dominant contributions to the right side of Eq. (39) are the phonon cooling and Auger heating, which enter the first term. The second term is negligible, since particle numbers change relatively slowly. For short pulses both the ortho-to-para conversion and the Auger decay rates are proportional to $n_o \sim T^{3/2}$ along the phase boundary; the total decay rate is $\approx 1 \text{ ns}^{-1}$ for (ortho-exciton) density 10^{18} cm^{-3} .¹³ For the case of long pulses the net production rate (laser production minus decay processes) is even smaller. For small values of the chemical potential, therefore, the second term will be on the order of the kinetic energy times the decay rate, which is more than an order of magnitude smaller than the phonon cooling and the Auger heating rates. In addition, the final term is negligible for small expansion of the gas, which we have assumed.

The slow rate of change of particle numbers also allows us to relate the first term on the right side of Eq. (39) to the total change of the energy of the excitons (ortho plus para) by

$$\frac{1}{N_o} \frac{dE_o}{dt} = \frac{N}{N_o} \frac{C_o(T)}{C_o(T) + C_p(T)} \frac{1}{N} \frac{dE}{dt}, \quad (40)$$

where $C_i = (\partial E_i / \partial T)_{N_i, V}$ is the heat capacity of the i th component at constant volume and number of particles. For the

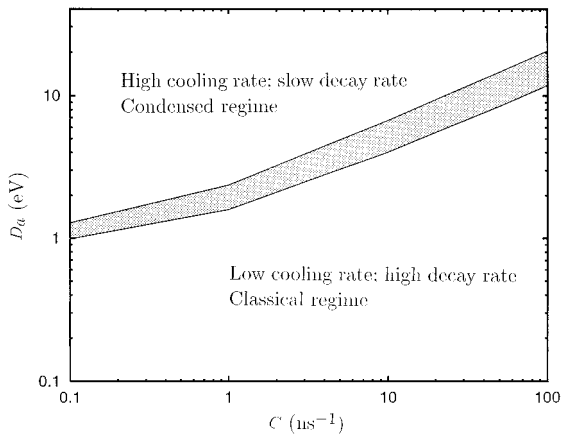


FIG. 21. The shaded region shows the range of the values of the Auger heating parameter C and the magnitude of the acoustic-phonon deformation potential D_a , which gives the observed quantum saturation of the ortho excitons.

excitons close to the Bose-Einstein condensation phase boundary, $C_p/C_o \approx N_p/N_o$, so that $(1/N_o)(dE_o/dt) \approx (1/N)(dE/dt)$.

The acoustic-phonon cooling rate per exciton, for excitons with $\alpha = 0.15$, is $\approx -0.56T^{3/2}(1 - T_\ell/T) \text{ meV/ns}$ [cf. Fig. 4(a)]. Since we are interested in $T \gg T_\ell$, we neglect the term T_ℓ/T .

In the case of short-pulse excitation, the para-exciton density is approximately constant, $\approx 10^{19} \text{ cm}^{-3}$, due to a balance between the ortho-to-para conversion process and the Auger loss of para excitons. Since the Auger heating of ortho excitons per particle is a function of the total exciton density ($\geq 10^{19} \text{ cm}^{-3}$), we assume that $E_A \approx 0.77E_b$ [cf. Fig. 10] and neglect its weak density dependence. Then the Auger heating rate per particle varies approximately as $11.8n_o \text{ meV/ns}$ with n_o measured in units of 10^{18} cm^{-3} . For the case of long-pulse excitation, the Auger heating is a bit smaller, closer to $E_A \approx 0.64E_b$, since the total density is smaller in this case, but still the density dependence of E_A is weak for $n \geq 5 \times 10^{18} \text{ cm}^{-3}$.

With these approximations Eq. (39) takes the form

$$T \frac{ds_o}{dt} \approx -aT^{3/2} + bn_o, \quad (41)$$

where, for T in kelvin and n_o in units of 10^{18} cm^{-3} , $a \approx 0.56 \text{ meV/ns}$, and $b \approx 11.8 \text{ meV/ns}$ for short pulses and $\approx 9.8 \text{ meV/ns}$ for long pulses. Note that the right side of Eq. (41) vanishes on the adiabat for which, in the same units, $n_o \approx 0.048T^{3/2}$ for short pulses, and $n_o \approx 0.058T^{3/2}$ for long pulses, and that this equation predicts that the ortho excitons approach this adiabat as a stable fixed point. The adiabat of stability, as calculated approximately here, is shown as a dash-dot line in Fig. 11 for short-pulse excitation and Fig. 15 for long-pulse excitation.

To calculate the characteristic time τ_* for the ortho excitons to approach the adiabat of stability, we regard Eq. (41) as an equation for α . Near this adiabat, on which $\alpha \equiv \alpha_*$,

$$\frac{d\alpha}{dt} = -\frac{\alpha - \alpha_*}{\tau_*}, \quad (42)$$

where

$$\tau_* = -\frac{T}{b} \left(\frac{\partial s_o}{\partial n_o} \right)_T \approx \frac{5\zeta(5/2)}{2\zeta(3/2)} \frac{k_B}{aT^{1/2}}; \quad (43)$$

the latter form holds near the phase boundary. Numerically $\tau_* \approx 0.20T^{-1/2} \text{ ns}$, with T measured in kelvin. In the case of short-pulse excitation, for $T = 60 \text{ K}$, $\tau_* \approx 25 \text{ ps}$. The present data are consistent with the predicted approach to the adiabat of stability, but since the photoluminescence time resolution in the experiments, from 100 to 300 ps, is much larger than τ_* , the approach cannot be verified in detail.

VII. SUMMARY

We have shown that the observed quantum saturation of ortho excitons is caused by a competition between the Auger process and the cooling of the excitons by the phonons. When the ortho excitons approach the phase boundary, these two mechanisms act together to keep the ortho excitons on a

particular adiabat, parallel, but at slightly higher temperature than the phase boundary. The cooling is affected by the proximity of the excitons to the phase boundary, but the Auger process is not significantly affected by the degeneracy of excitons. We find that there is a fairly wide range of numbers that can be inserted for the various parameters and still account for the observed quantum saturation effect. Reasonable changes in the parameter values cause the trajectories to shift relative to the phase boundary but do not qualitatively change the results. Also, the assumed laser profile and width do not change the results of our calculation appreciably. We have, however, made the assumption of a constant gas volume over the short time intervals considered (1–20 ns).

Our key finding is that, while the ortho excitons encounter a formidable barrier to condensation, the para excitons do indeed cross the phase boundary and condense. Specific features of the band structure of Cu_2O underlie this condensation. Earlier work has noted the simple parabolic bands and the forbidden direct gap. Our present study points out that para-exciton–para-exciton Auger collisions are very slow for both the direct and the phonon-assisted Auger processes. Details will be reported in Ref. 9. Finally, we remark that this analysis presents no fundamental reason why the ortho excitons cannot condense; however, their multiplicity, their faster Auger decay, and their conversion to para excitons make their condensation much more difficult than for para excitons.

ACKNOWLEDGMENTS

The work of G.M.K. and G.B. was supported by NSF Grants Nos. DMR91-22385 and PHY94-21309, and that of J.P.W. by NSF Grant No. DMR92-07458. Helpful comments from Y.C. Chang, K. O’Hara, L. O’Suilleabhain, and D.W. Snoke are gratefully acknowledged. G.M.K. wishes to thank the Research Center of Crete, Greece for its hospitality.

APPENDIX: CALCULATION OF ELECTRON (OR HOLE) EXCITON SCATTERING MATRIX ELEMENT

We calculate here the matrix element $M_{\mathbf{q}}^{\text{ce}}$ for scattering of an electron or hole by an exciton [Fig. 9(b)]. Consider an

electron of momentum \mathbf{k} and an exciton of momentum \mathbf{p} scattering into $\mathbf{k}-\mathbf{q}$ and $\mathbf{p}+\mathbf{q}$, respectively. The electron (or hole) exciton interaction is

$$\mathcal{V} = \frac{e^2}{\epsilon_0} \left(\frac{1}{|\mathbf{r}-\mathbf{r}_e|} - \frac{1}{|\mathbf{r}-\mathbf{r}_h|} \right), \quad (\text{A1})$$

where \mathbf{r} is the position of the electron (or hole) and \mathbf{r}_e and \mathbf{r}_h are the positions of the bound electron and hole, respectively. The wave functions of the initial and final states are

$$\begin{aligned} \psi_i &= \frac{1}{\sqrt{V}} e^{i\mathbf{k}\cdot\mathbf{r}} \Psi_{\mathbf{p}}(\mathbf{r}_e - \mathbf{r}_h), \\ \psi_f &= \frac{1}{\sqrt{V}} e^{i(\mathbf{k}-\mathbf{q})\cdot\mathbf{r}} \Psi_{\mathbf{p}+\mathbf{q}}(\mathbf{r}_e - \mathbf{r}_h), \end{aligned} \quad (\text{A2})$$

where

$$\Psi_{\mathbf{p}}(\mathbf{r}_e - \mathbf{r}_h) = \frac{1}{\sqrt{V}} e^{i\mathbf{p}\cdot(\lambda_e\mathbf{r}_e + \lambda_h\mathbf{r}_h)} \Phi_{\text{rel}}(\mathbf{r}_e - \mathbf{r}_h) \quad (\text{A3})$$

is the exciton wave function with center-of-mass momentum \mathbf{p} , and $\Phi_{\text{rel}}(\mathbf{r}_e - \mathbf{r}_h)$ is the wave function of the relative motion. The matrix element of the interaction between the initial and final states is thus

$$M_{\mathbf{q}}^{\text{ce}} = \frac{4\pi e^2}{\epsilon_0 V q^2} \left[\frac{1}{[1 + (qa\lambda_h/2)^2]^2} - \frac{1}{[1 + (qa\lambda_e/2)^2]^2} \right]. \quad (\text{A4})$$

The factor inside the parentheses comes again from the Fourier transform of the relative electron-hole wave function, which we assume to be the $1s$ state. In the limit $\lambda_e \approx \lambda_h$,

$$M_{\mathbf{q}}^{\text{ce}} \approx \frac{2\pi e^2 a^2}{\epsilon_0 V} \frac{(\lambda_e - \lambda_h)}{[1 + (qa/4)^2]^3}. \quad (\text{A5})$$

¹ T.J. Greytak and D. Kleppner, in *New Trends in Atomic Physics*, edited by G. Grynberg and R. Stora (North-Holland Publishers, Amsterdam, 1984).
² *Bose Einstein Condensation*, edited by A. Griffin, D.W. Snoke, and S. Stringari (Cambridge University Press, Cambridge, 1995).
³ M.H. Anderson, J.R. Ensher, M.R. Matthews, C.E. Wieman, and E.A. Cornell, *Science* **269**, 198 (1995); C.C. Bradley, C.A. Sackett, J.J. Tollett, and R.G. Hulet, *Phys. Rev. Lett.* **75**, 1687 (1995); K.B. Davis, M.-O. Mewes, M.R. Andrews, N.J. van Druten, D.S. Durfee, D.M. Kurn, and W. Ketterle, *Phys. Rev. Lett.* **75**, 3969 (1995).
⁴ D. Hulin, A. Mysyrowicz, and C. Benoît à la Guillaume, *Phys. Rev. Lett.* **45**, 1970 (1980); A. Mysyrowicz, D. Hulin, and C. Benoît à la Guillaume, *J. Lumin.* **24/25**, 629 (1981).

⁵ D.W. Snoke, J.P. Wolfe, and A. Mysyrowicz, *Phys. Rev. Lett.* **59**, 827 (1987).
⁶ D.W. Snoke, J.P. Wolfe, and A. Mysyrowicz, *Phys. Rev. Lett.* **64**, 2543 (1990); *Phys. Rev. B* **41**, 11 171 (1990).
⁷ J.-L. Lin and J.P. Wolfe, *Phys. Rev. Lett.* **71**, 1223 (1993).
⁸ V.A. Kiselev and A.G. Zhilich, *Fiz. Tverd. Tela* **13**, 2398 (1971) [*Sov. Phys. Solid State* **13**, 2008 (1972)]; M.M. Denisov and V.P. Makarov, *Phys. Status Solidi B* **56**, 9 (1973); V.P. Makarov, *Zh. Eksp. Teor. Fiz.* **54**, 324 (1968) [*Sov. Phys. JETP* **27**, 173 (1968)]; G.E. Pikus and G.L. Bir, *ibid.* **60**, 195 (1971) [*ibid.* **33**, 108 (1971)].
⁹ G.M. Kavoulakis and G. Baym (unpublished).
¹⁰ We note, however, that even in the stressed case, the para-exciton spectrum is not completely explained. Its nonzero width and slight blueshift have been modeled by H. Shi, G. Verchaka, and

- A. Griffin [Phys. Rev. B **50**, 1119 (1994)] in terms of many-body interactions within the gas. Understanding this spectrum remains one of the outstanding problems of the quantum-degenerate exciton system.
- ¹¹ D.W. Snoke, D.P. Trauernicht, and J.P. Wolfe, Phys. Rev. B **41**, 5266 (1990).
- ¹² F.I. Kreingol'd and V.L. Makarov, Fiz. Tverd. Tela **15**, 1307 (1973) [Sov. Phys. Solid State **15**, 890 (1973)]; J.S. Weiner, N. Caswell, P.Y. Yu, and A. Mysyrowicz, Solid State Commun. **46**, 105 (1989).
- ¹³ D.W. Snoke and J.P. Wolfe, Phys. Rev. B **42**, 7876 (1990); D.P. Trauernicht, J.P. Wolfe, and A. Mysyrowicz, Phys. Rev. B **34**, 2561 (1986).
- ¹⁴ B. Link and G. Baym, Phys. Rev. Lett. **69**, 2959 (1992).
- ¹⁵ J. Bardeen and W. Shockley, Phys. Rev. **80**, 72 (1950).
- ¹⁶ K. Seeger, in *Semiconductor Physics: An Introduction*, edited by M. Cardona, P. Fulde, K. von Klitzing, and H.-J. Queisser, Springer Series in Solid-State Sciences Vol. 40 (Springer-Verlag, New York, 1991).
- ¹⁷ P.Y. Yu and Y.R. Shen, Phys. Rev. B **12**, 1377 (1975).
- ¹⁸ D.W. Snoke, D. Braun, and M. Cardona, Phys. Rev. B **44**, 2991 (1991).
- ¹⁹ M. O'Keefe, J. Chem. Phys. **39**, 1789 (1963).
- ²⁰ A.G. Zhilich, J. Halpern, and B.P. Zakharchenya, Phys. Rev. **188**, 1294 (1969).
- ²¹ J.W. Hodby, T.E. Jenkins, C. Schwab, H. Tamura, and D. Trivich, J. Phys. C **9**, 1429 (1976); T. Itoh and S. Narita, J. Phys. Soc. Jpn. **39**, 132 (1975).
- ²² C. Carabatos and B. Prevot, Phys. Status Solidi B **44**, 701 (1971); K. Reimann and K. Syassen, Phys. Rev. B **39**, 11 113 (1989).
- ²³ D.P. Trauernicht and J.P. Wolfe, Phys. Rev. B **33**, 8506 (1986).
- ²⁴ E.O. Kane, in *Physics of III-IV Compounds*, edited by R.K. Willardson and A.C. Beer, Semiconductors and Semimetals Vol. 1 (Academic Press, New York, 1966), p. 75.
- ²⁵ P.L. Gourley and J.P. Wolfe, Phys. Rev. B **24**, 5970 (1981); H. Yoshida, H. Saito, and S. Shionoya, Phys. Status Solidi B **104**, 331 (1981).
- ²⁶ A.R. Beattie and P.T. Landsberg, Proc. R. Soc. London Ser. A **249**, 16 (1958); B.K. Ridley, in *Quantum Processes in Semiconductors* (Clarendon Press, Oxford, 1982); A. Haug, Solid State Commun. **22**, 537 (1977); A. Das and R. Al-Jishi, Phys. Lett. A **141**, 186 (1989); A. Haug, Solid State Electron. **21**, 128 (1978).
- ²⁷ J.P. Dahl and A.C. Switendick, J. Phys. Chem. Solids **27**, 931 (1965); R.J. Elliott, Phys. Rev. **124**, 340 (1961); L. Kleinman and K. Mednick, Phys. Rev. B **21**, 1549 (1980).
- ²⁸ S.E. Esipov, M. Msall, and J.P. Wolfe, Phys. Rev. B **47**, 13 330 (1993).
- ²⁹ E. Hanamura and H. Haug, Phys. Rep. C **33**, 209 (1977).